Dynamical evidence for a morphology-dependent relation between the stellar and halo masses of galaxies

Lorenzo Posti, S. Michael Fall

A&A 649, A119 (2021)
https://doi.org/10.1051/0004-6361/202040256

Astronomy & Astrophysics

Dynamical evidence for a morphology-dependent relation between the stellar and halo masses of galaxies

L. Posti[1] and S. M. Fall[2]

[1] Université de Strasbourg, CNRS UMR 7550, Observatoire Astronomique de Strasbourg, 11 Rue de l'Université, 67000 Strasbourg, France
e-mail: lorenzo.posti@astro.unistra.fr
[2] Space Telescope Science Institute, 3700 San Martin Drive, Baltimore, MD 21218, USA

Received 28 December 2020 / Accepted 22 February 2021

ABSTRACT

We derive the stellar-to-halo mass relation (SHMR), namely $f_\star \propto M_\star/M_\mathrm{h}$ versus $M_\star$ and M_h, for early-type galaxies from their near-infrared luminosities (for $M_\star$) and the position-velocity distributions of their globular cluster systems (for M_h). Our individual estimates of M_h are based on fitting a flexible dynamical model with a distribution function expressed in terms of action-angle variables and imposing a prior on M_h from the correlation between halo concentration and mass in the standard Λ cold dark matter (ΛCDM) cosmology. We find that the SHMR for early-type galaxies declines with mass beyond a peak at $M_\star \sim 5\times10^{10}\,M_\odot$ and $M_\mathrm{h} \sim 1\times10^{12}\,M_\odot$ (near the mass of the Milky Way). This result is consistent with the standard SHMR derived by abundance matching for the general population of galaxies, and also with previous, less robust derivations of the SHMR for early-type galaxies. However, it contrasts sharply with the monotonically rising SHMR for late-type galaxies derived from extended HI rotation curves and the same ΛCDM prior on M_h that we adopt for early-type galaxies. We show that the SHMR for massive galaxies varies more or less continuously with disc fraction and Hubble type between these rising and falling branches. We also show that the different SHMRs for late-type and early-type galaxies are consistent with the similar scaling relations between their stellar velocities and masses (the Tully–Fisher and the Faber–Jackson relations). As we demonstrate explicitly, differences in the relations between the stellar and halo virial velocities account for the similarity of the scaling relations. We argue that all these empirical findings are natural consequences of a picture in which galactic discs are built mainly by relatively smooth and gradual inflow, regulated by feedback from young stars, while galactic spheroids are built by a combination of merging, black-hole fuelling, and feedback from active galactic nuclei.

Key words. galaxies: kinematics and dynamics – galaxies: elliptical and lenticular, cD – galaxies: spiral – galaxies: structure – galaxies: formation

1. Introduction

Galaxies consist of stars and interstellar gas in relatively compact bodies surrounded by more extended halos of dark matter and circumgalactic gas. The composition of the dark matter is unknown, but it is believed to be elementary particles that interact only gravitationally with baryons. In the standard Λ cold dark matter (ΛCDM) paradigm, the assembly of galactic halos by gravitational clustering is relatively simple and well understood, while the inflow and outflow of gas and the formation of stars by both gravitational and hydrodynamical processes are much more complex and are topics of intense current research. One of the most useful empirical constraints in these studies – and the focus of this paper – is the ratio of the mass in stars $M_\star$ to that in dark matter M_h within a galaxy normalised by the cosmic baryon fraction f_b:

$$f_\star \equiv \frac{M_\star}{f_\mathrm{b} M_\mathrm{h}}. \tag{1}$$

This ratio represents a sort of global star formation efficiency, averaged over space and time, for that galaxy.

The variation of $f_\star$ with $M_\star$ or M_h is called the stellar-to-halo mass relation (SHMR). This has now been derived using several different techniques: abundance matching (Vale & Ostriker 2004; Conroy et al. 2006; Behroozi et al. 2013; Moster et al. 2013), halo occupation distributions (Peacock & Smith 2000; Kravtsov et al. 2004; Reddick et al. 2013), group catalogues (Zheng et al. 2007; Yang et al. 2008), weak galaxy-galaxy lensing (Leauthaud et al. 2012; van Uitert et al. 2016), galaxy clustering (Zu & Mandelbaum 2015; Tinker et al. 2017), and empirical models (Rodríguez-Puebla et al. 2017; Moster et al. 2018; Behroozi et al. 2019). The consensus of these studies is that $f_\star$ increases with mass to a peak, with $f_\star \sim 20\%$ at $M_\star \sim 5\times10^{10}\,M_\odot$ and $M_\mathrm{h} \sim 10^{12}\,M_\odot$ (near the mass of the Milky Way), and then decreases with mass.

The standard explanation for the inverted-U shape of the SHMR is that feedback by young stars is responsible for the low-mass part, while feedback from active galactic nuclei (AGN) is responsible for the high-mass part. Both types of feedback are potentially capable of driving outflows from a galaxy and impeding further inflows, thus quenching star formation. The effect of stellar feedback on the SHMR is fairly well understood; a higher fraction of gas is driven out of low-mass galaxies because they have lower escape speeds (e.g. Dekel & Silk 1986; Veilleux et al. 2005). Near the peak of the SHMR, much of the gas probably circulates in a self-regulated fountain without escaping from the halo (Tumlinson et al. 2017, and references therein). The effect of AGN feedback on the SHMR is less well understood, but it is plausible that it drives energetic outflows that heat some of the circumgalactic gas, thus slowing or reversing its inflow (e.g. Fabian 2012; King & Pounds 2015; Harrison 2017). Mergers may also disrupt the inflow and

quench star formation, at least temporarily (e.g. Hopkins et al. 2010a). Both mergers and AGN feedback may work together to cause the decline of the SHMR at high masses (e.g. Croton et al. 2006) since mergers can funnel gas to a central black hole, igniting AGN feedback (e.g. Hopkins et al. 2006) while also building galactic spheroids (i.e. classical bulges; Hopkins et al. 2010b).

In practice, the SHMR is usually assumed to be independent of galactic morphology (Wechsler & Tinker 2018). This assumption, however, appears to contradict the reasoning above about the different roles of stellar and AGN feedback and the observation that the masses of central black holes correlate with the bulge masses of their host galaxies (Kormendy & Ho 2013). Thus, if AGN feedback is important, it should have more effect on the high-mass shape of the SHMR for bulge-dominated galaxies than it does for disc-dominated galaxies. More specifically, $f_\star$ should decline with $M_\star$ and M_h past the peak in early-type galaxies but rise or level off in late-type galaxies. The main goals of this paper are to confirm this expected dependence of the SHMR on galaxy morphology and to explore some of its implications for our understanding of galaxy formation.

There is already some evidence for secondary correlations between the SHMR and other properties of galaxies. This evidence comes from weak lensing (Mandelbaum et al. 2006, 2016; Tinker et al. 2013; Hudson et al. 2015; Taylor et al. 2020), satellite kinematics (Conroy et al. 2007; More et al. 2011; Wojtak & Mamon 2013; Lange et al. 2019), empirical models (Rodríguez-Puebla et al. 2015), abundance matching (Hearin et al. 2014; Saito et al. 2016), or a combination of these methods (Dutton et al. 2010). The results of these studies are consistent with the expectation that early-type galaxies occupy more massive halos than late-type galaxies of the same stellar mass. However, in most cases, the results are based on stacking the observations in large samples of galaxies to amplify the marginal or undetectable signals from individual galaxies, an approach that can sometimes yield spurious correlations (and has led to some debate on the topic; see Sect. 6.1 in Wechsler & Tinker 2018). Some recent hydrodynamical simulations also display the expected differences between the SHMRs of early-type and late-type galaxies (Grand et al. 2019; Marasco et al. 2020; Correa & Schaye 2020).

The most direct approach to deriving the SHMR is to estimate the masses of individual halos from the observed kinematics of tracer objects whose space distribution extends well beyond the luminous parts of galaxies. Since the available tracers almost never reach the expected outer (virial) radii of the halos, estimates of their total masses require priors such as the correlation between concentration and mass found in ΛCDM simulations. This is the approach taken by Posti et al. (2019a, hereafter PFM19) to derive the SHMR of 110 late-type galaxies with extended HI rotation curves in the *Spitzer* Photometry and Accurate Rotation Curves (SPARC) sample (Lelli et al. 2016a)[1]. PFM19 found that the SHMR rises monotonically for all masses and reaches $f_\star \sim 0.3{-}1$ for the most massive galaxies in this sample, with $M_\star \sim 1{-}3\times10^{11}\,M_\odot$ (dubbed the 'failed feedback problem'). This result is in stark contrast to the declining high-mass form of the SHMR found in most studies of the general population of galaxies, which is dominated by early types at the highest masses (Kelvin et al. 2014).

In this paper, we derive the SHMR for early-type galaxies by methods as similar as possible to those used by PFM19 for late-type galaxies. In particular, we adopt the same ΛCDM correlation between halo concentration and mass. However, instead of using HI rotation curves to probe the gravitational potential, we use the radial velocities of globular clusters (GCs) around 25 massive early-type galaxies in the SAGES Legacy Unifying Globulars and GalaxieS Survey (SLUGGS, Brodie et al. 2014). We fit a distribution function, expressed in terms of action and angle variables, to the observed kinematics and space distribution of each GC system to estimate its halo mass. This enables us, for the first time, to make a direct and robust comparison between the SHMR of early types and late types based on individual estimates of halo masses.

The different SHMRs for early-type and late-type galaxies – one with a prominent bend, the other without – may seem puzzling because both galactic types have similar scaling relations between stellar velocities and masses (the Faber–Jackson and Tully–Fisher relations). Since the SHMR and the velocity scaling relations both depend on $M_\star$, one might reasonably expect a bend in the former to impose a bend in the latter. However, since the SHMR also depends on M_h, it is possible that the similar velocity scaling relations are actually explained by, and disguised by, different underlying relations between the stellar velocities of early-type and late-type galaxies and one or more properties of their dark matter halos, thus offering potentially important clues about the physical mechanisms responsible for different galactic morphologies. We explore this issue here for the first time.

The remainder of this paper is organised as follows. In Sect. 2, we summarise the data and dynamical models we use to estimate M_h for early types and the analogous estimates of M_h from PFM19 for late types. Interested readers can find a full description of our models for early-type galaxies in Appendix A. In Sect. 3, we present our SHMR, showing unambiguously that it depends on galaxy morphology and disc fraction. Section 4 compares our results with previous evidence for different SHMRs. In Sect. 5, we reconcile the different shapes of the SHMRs for late-type and early-type galaxies with their similar velocity scaling relations in terms of differences between their stellar and halo velocities, and we interpret this result as a natural consequence of the different roles of smooth inflow, merging, and AGN feedback in the formation of galactic discs and spheroids. Section 6 summarises our main conclusions.

Throughout the paper, we use a fixed critical overdensity parameter $\Delta = 200$ to define the virial quantities of dark matter halos and a standard ΛCDM model with a Hubble constant $H_0 = 67.4\,\mathrm{km\,s^{-1}\,Mpc^{-1}}$ and a cosmic baryon fraction $f_\mathrm{b} = \Omega_\mathrm{b}/\Omega_\mathrm{m} = 0.156$ (Planck Collaboration VI 2020). We distinguish between late-type and early-type galaxies based on published morphological classifications; early types are E and S0 (Hubble type $T < 0$), while late types are S0/a, Sa, Sb, Sc, and Irr (Hubble type $T \geq 0$).

2. Dynamical estimates of halo masses for early-type and late-type galaxies

2.1. Early types

The main novelty of this work is our dynamical estimates of halo masses (M_h) for individual nearby ellipticals and lenticulars. To derive these, we use observations of the kinematics of the GC systems around these galaxies, and we model explicitly their distribution function. Our method is an adaptation of that of Posti & Helmi (2019), who used it to measure the halo mass of the Milky Way. The method consists of two main ingredients: the distribution function (DF) of the GC system and the gravitational potential. Here we provide an overview of our method with the guidance of Fig. 1, which illustrates the input, fitting,

[1] In this context, HI is a better tracer than Hα because it usually extends to larger radii (van Albada et al. 1985; Kent 1986, 1987).

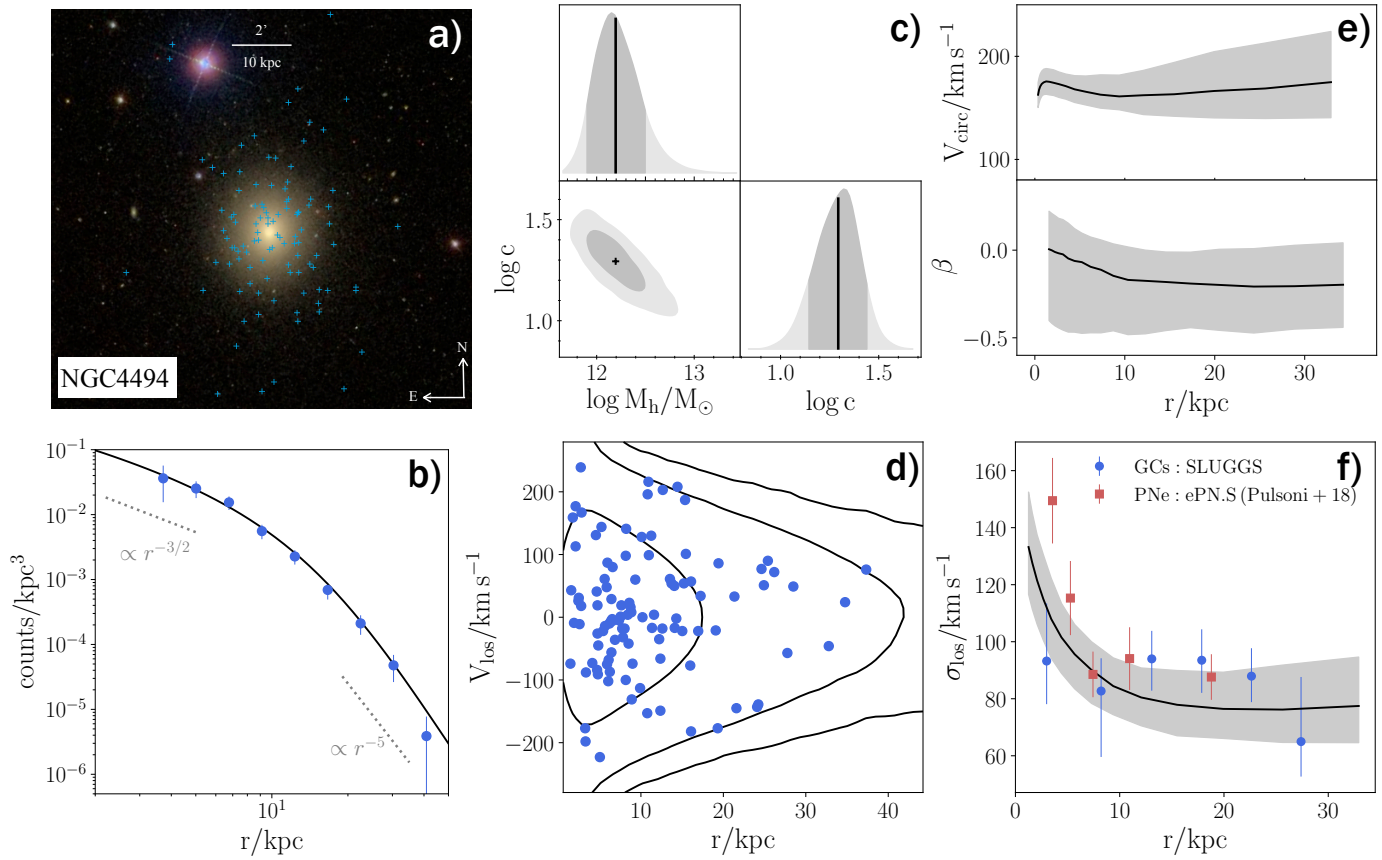

Fig. 1. Illustration of our modelling technique using NGC 4494 as an example. In all panels, GC data are shown as blue points, the DF model is shown as a black solid curve, and the 68% confidence interval of the model is shown as a grey shaded area. *a*: Sloan Digital Sky Survey (SDSS) colour image of the galaxy with blue crosses marking the spectroscopically confirmed GCs in the SLUGGS survey (made with `Aladin`). *b*: projected number density profile of the GCs compared to that of the $f(\boldsymbol{J})$ model. *c*: marginalised posterior distributions of the halo mass and concentration estimated with an MCMC method. Dark and light grey areas encompass, respectively, 68% and 95% probability, while the black solid lines and cross mark the maximum-likelihood model. *d*: LOS velocity as a function of projected radius, $V_{los}-r$, for the GCs compared with the projected phase-space density of the maximum-likelihood $f(\boldsymbol{J})$ model. The contours contain 68–95–99% of the projected phase-space density of the model. *e*: circular velocity profile, V_{circ} (*top*), and velocity anisotropy profile, $\beta = 1 - (\sigma_\theta^2 + \sigma_\phi^2)/2\sigma_r^2$ (*bottom*), of the $f(\boldsymbol{J})$ model. *f*: LOS velocity dispersion profile of the GCs measured with SLUGGS data compared to that of our $f(\boldsymbol{J})$ model. We also compare to independent measurements of the σ_{los} profile of planetary nebulae from Pulsoni et al. (2018, red squares).

and output of our model for a representative galaxy, NGC 4494. This section introduces all the information needed to understand our results, while Appendix A provides a detailed description of our model, which the busy reader can skip. We report the numerical output of our model for all the early-type galaxies in our sample in Appendix B.

Data. We take the velocity and position data of the GC systems around 27 nearby bright ellipticals and lenticulars from the SLUGGS Survey (Brodie et al. 2014). The centrepiece of this data set is the catalogue of radial velocities of the spectroscopically confirmed GCs obtained with DEIMOS@Keck (Forbes et al. 2017a). Each galaxy has tens or hundreds of GCs, with a significant galaxy-to-galaxy variation, and with a typical uncertainty on each radial velocity of about ∼10−20 km s^{-1}. The radial coverage of the GC system is also quite varied: The radius containing 90% of the observed GCs ranges between 8 and 98 kpc (corresponding to $3R_e$ and $14R_e$) with a median of about 30 kpc (corresponding to $7.5R_e$). The top panel of Fig. 2 shows the distributions of the median radii ($R_{med,GC}$) and the outermost radii ($R_{last,GC}$) of the GC systems, both normalised by the effective radii of the galaxies (R_e). To model the distribution of baryons, we use the photometric profiles derived from *Spitzer* Space Telescope images at 3.6 µm by Forbes et al. (2017b). Out of the 27 galaxies in Brodie et al. (2014), we exclude NGC 4474, since it does not have *Spitzer* images, and NGC 4111, since it has fewer than 20 GC velocities. As an example, in Fig. 1a, we show the distribution of the confirmed SLUGGS GCs around NGC 4494.

Distribution function. We use analytic DFs that depend on action-angle variables in the form introduced by Posti et al. (2015) specifically to describe spheroidal systems. We refer to these models as $f(\boldsymbol{J})$, where f is the DF and $\boldsymbol{J}$ are the actions. The models we use have spherical space distributions but anisotropic velocity distributions. The DFs are double power laws in the actions such that they generate double power-law density distributions in physical space. Once the two slopes of the DF are fitted to the space distributions of GCs (Fig. 1b), the three remaining parameters specify the velocity distribution of the GC system.

Gravitational potential. The total potential in the $f(\boldsymbol{J})$ model is a superposition of two spherical components: the luminous galaxy and the dark matter halo. The galaxy is modelled as a de-projected Sersic (1968) profile, based on the photometry by Forbes et al. (2017a), with an adjustable mass-to-light ratio. The dark matter halo is assumed to have a Navarro et al. (1996,

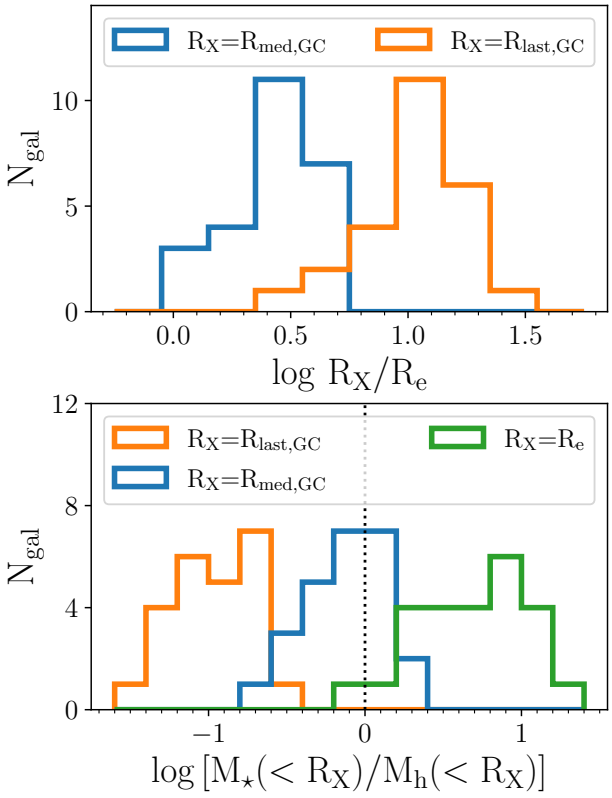

Fig. 2. Radial coverage of the GC systems and ratios of stellar-to-halo mass enclosed within progressively larger radii for early-type galaxies in SLUGGS. *Top panel*: distributions of the median radii ($R_{\rm med,GC}$, blue) and of the outermost radii ($R_{\rm last,GC}$, orange) of the GC systems around the early types in SLUGGS. Both radii are normalised to the effective radius of the luminous galaxy ($R_{\rm e}$). *Bottom panel*: distributions of the ratios of stellar-to-halo mass enclosed within the effective radius ($R_{\rm e}$, green), within the median GC radius ($R_{\rm med,GC}$, blue), and within the outermost GC radius ($R_{\rm last,GC}$, orange). These are computed from the best-fit $f(\boldsymbol{J})$ model of each galaxy. The dotted vertical line separates the regions where the dark matter dominates (*left*) and where the stars dominate (*right*).

herafter NFW) profile parametrised by its virial mass ($M_{\rm h}$) and concentration (c). For the mass-to-light ratio, we impose a Gaussian prior with a mean derived by Forbes et al. (2017a), using stellar population models, and a dispersion $\sigma_{\log(\rm M/L)} = 0.2$ dex. For the halo concentration, we impose the correlation between c and $M_{\rm h}$ found in N-body ΛCDM simulations (Dutton & Macciò 2014).

Bayesian parameter estimation. We use a Markov chain Monte Carlo (MCMC) method to derive posterior probabilities of the free parameters of our model (Fig. 1c). The likelihood is given by the product of the DF convolved by the error distribution for each cluster. Since we need three positions and three velocities to evaluate the DF, we sample the missing position from the observed density distribution of the clusters and the two missing velocities uniformly in the range allowed by the escape speed of the model (Fig. 1d). We then use our $f(\boldsymbol{J})$ models to derive the intrinsic properties of the potential (the circular velocity $V_{\rm circ}$) and of the GC system (the anisotropy parameter $\beta = 1 - (\sigma_\theta^2 + \sigma_\phi^2)/2\sigma_{\rm r}^2$) shown in Fig. 1e. In the bottom panel of Fig. 2, we use the $f(\boldsymbol{J})$ models to compute the ratios of stellar-to-halo mass enclosed within progressively larger radii: the luminous $R_{\rm e}$, the median GC radius $R_{\rm med,GC}$, and the outermost GC radius $R_{\rm last,GC}$. Evidently, dark matter is negligible relative to stars near $R_{\rm e}$, is comparable near $R_{\rm med,GC}$ (∼2−4$R_{\rm e}$), and is dominant near $R_{\rm last,GC}$ (∼5−20$R_{\rm e}$). We can also compute a posteriori the model line-of-sight (LOS) velocity dispersion profile and check that it is consistent with the observed profile for GCs in the SLUGGS Survey and planetary nebulae in the ePN.S Survey (Pulsoni et al. 2018). Figure 1f shows this consistency for NGC 4494.

2.2. Late types

PFM19 estimated the halo masses for a sample of nearby spirals by fitting galaxy plus halo models to their extended HI rotation curves. Here we just summarise their analysis and results and refer the reader to their paper for full details.

Data. The sample consists of 110 nearby spirals with 3.6 µm *Spitzer* images and HI rotation curves drawn from the SPARC database compiled by Lelli et al. (2016a, and references therein). The rotation curves, taken from various sources in the literature, were derived from interferometric HI observations that extended well beyond the optical discs of the galaxies. The sample spans a large range in stellar masses, from dwarfs ($M_\star \sim 10^7\,M_\odot$) to giants ($M_\star \sim 10^{11}\,M_\odot$).

Rotation curve decomposition. The observed rotation curves are decomposed into gas, stars, and dark matter components. The gas contribution is derived directly from the HI flux, while the stellar contribution is computed from the 3.6 µm photometry with an adjustable mass-to-light ratio. The dark matter halo is modelled as a standard NFW profile with variable virial mass ($M_{\rm h}$) and concentration (c) following the c−$M_{\rm h}$ relation from ΛCDM simulations (Dutton & Macciò 2014). In massive spirals, which are the focus of this work, models with cuspy dark matter halos (such as NFW) match the observed rotation curves well, yielding fits that are statistically indistinguishable from those obtained with other halo models (e.g. pseudo-isothermal or cored halos; see de Blok et al. 2008; Martinsson et al. 2013; Katz et al. 2017; PFM19; Li et al. 2020). This contrasts with the situation for dwarf galaxies, whose rotation curves are often matched better by cored halo models (e.g. de Blok et al. 2001; Oh et al. 2011).

Bayesian parameter estimation. The MCMC approach is used to fit the rotation curve and to estimate the posterior distribution of the three free parameters of the gravitational potential: the stellar mass-to-light ratio, halo mass, and halo concentration. The marginalised posteriors of the three parameters are all unimodal.

It is important to note here that the key assumptions of the dynamical models for late types and early types are the same: an adjustable mass-to-light ratio at 3.6 µm, a spherical NFW halo, a prior following the ΛCDM c−$M_{\rm h}$ relation and an MCMC approach to sample the posterior. This makes the results from our $f(\boldsymbol{J})$ models for early-type galaxies directly comparable with those of PFM19 for late-type galaxies.

3. The SHMR for different galaxy types

3.1. Dependence on stellar and halo masses

In Fig. 3, we plot our estimates of $f_\star$ versus stellar mass $M_\star$ (left panel) and halo mass $M_{\rm h}$ (right panel) for the 25 SLUGGS early-type galaxies. We compare these with the estimates of $f_\star$ from PFM19 for SPARC late-type galaxies and with the abundance matching model of Moster et al. (2013). We find that, at a fixed

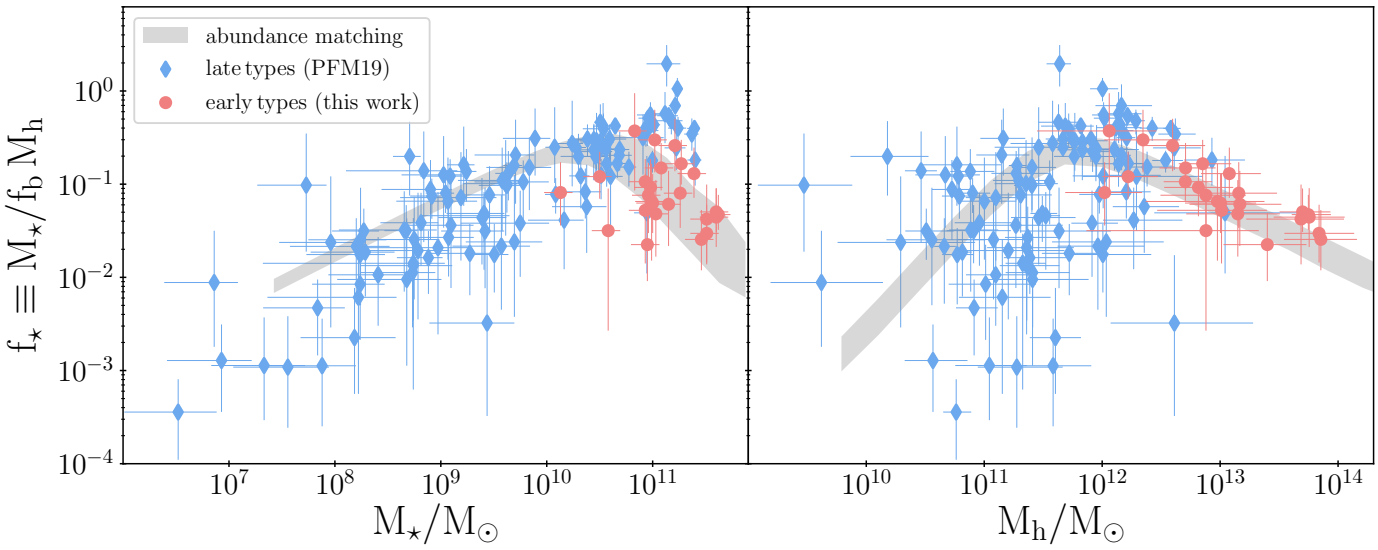

Fig. 3. SHMR in the form of the ratio $f_\star \equiv M_\star/f_b M_h$ as a function of stellar mass (*left*) and halo mass (*right*) for the sample of spiral galaxies in SPARC (blue diamonds, PFM19) and for the sample of ellipticals and lenticulars in SLUGGS (red circles, this work). The halo masses of late types are estimated from HI rotation curves, those of early types from the kinematics of the GC system. For comparison, we show also the abundance matching SHMR from Moster et al. (2013, grey band).

stellar mass above $\sim 5\times10^{10}\,M_\odot$, early types have systematically lower $f_\star$ than late types of similar stellar mass, by a factor of $\sim$7 at $M_\star \sim 10^{11}\,M_\odot$.

In order to guard against the possibility that the trends visible in Fig. 3 are induced by correlated errors in the plotted variables, $M_\star/M_h$ versus $M_\star$ or M_h, we also show in Fig. 4 the SHMR directly in the form $M_\star$ versus M_h. In particular, we zoom in on the high-mass regime of the SHMR ($M_\star > 10^{10}\,M_\odot$), which is of most interest here. Figure 4 confirms that late types and early types are separated from each other in the same way as indicated in Fig. 3; massive late types occupy systematically less massive halos than early types of the same stellar mass.

The grey bands in Figs. 3 and 4, representing the conventional SHMR derived by abundance matching, are displayed only for comparison purposes. We stress that all the main results of this paper come from dynamical analyses of late-type and early-type galaxies and do not depend in any way on abundance matching. In these figures, we show the SHMR from Moster et al. (2013) because it represents a consensus in the field (see Fig. 2 in Wechsler & Tinker 2018). In the SHMR derived by Kravtsov et al. (2018), massive galaxies tend to occupy slightly less massive halos with respect to the Moster et al. (2013) SHMR. However, even in this case, the qualitative picture presented in Figs. 3 and 4 remains valid.

For early types with $M_\star \gtrsim 10^{11}\,M_\odot$, we measure a scatter of $\approx$0.4 dex in $f_\star$ at a fixed $M_\star$. This scatter reflects a combination of several effects, which we assume to be independent to the first order: (i) the observational errors in the GC velocities and the uncertainty in the velocity dispersion due to sparse sampling, (ii) the uncertainty in the mass-to-light ratio, (iii) the scatter in the $c-M_h$ relation, and (iv) the intrinsic scatter in $f_\star$ at fixed $M_\star$. The first term varies substantially from galaxy to galaxy, as it is related to the signal-to-noise of the GC spectra and to the number of GCs observed, but for a typical galaxy this is of the order of 25%, or 0.1 dex. The second term is of the order of 0.1–0.2 dex (Forbes et al. 2017b). The third term is an output of cosmological simulations and is $\approx$0.11 dex (Dutton & Macciò 2014). The fourth term can be estimated from the conventional SHMR. We generate a population of halos from a standard halo mass function (Tinker et al. 2008) and we assign an $M_\star$ to each halo following the Moster et al. (2013) SHMR. They estimate the scatter of $f_\star$ to be 0.15 dex at a fixed halo mass M_h, which corresponds to the grey bands in $f_\star$ versus $M_\star$ and M_h in Fig. 3, and in $M_\star$ versus M_h in Fig. 4. The resulting scatter at a fixed stellar mass $M_\star$ is about 0.08 dex below the turnover at $M_\star \sim 5\times10^{10}\,M_\odot$ but then increases

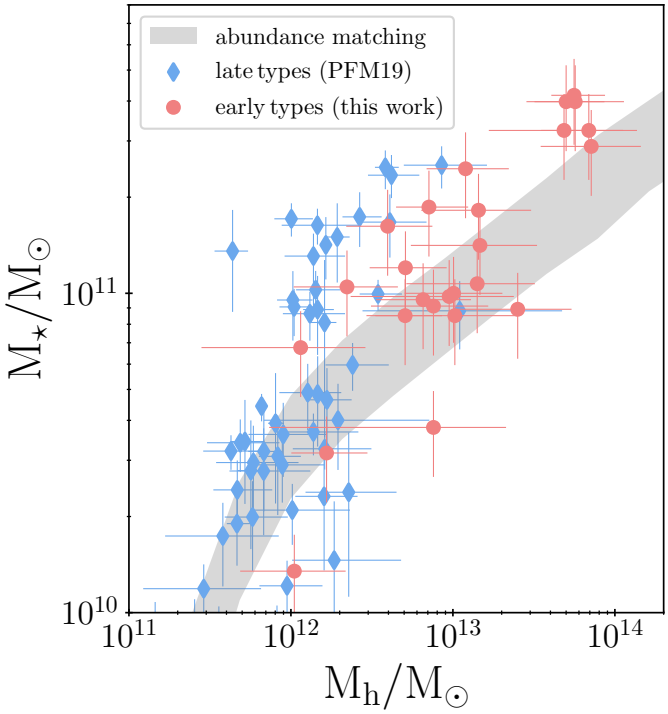

Fig. 4. SHMR in the form of stellar mass ($M_\star$) as a function of halo mass (M_h). The symbols are the same as in Fig. 3; however, here we zoom in on the high-mass regime of the SHMR.

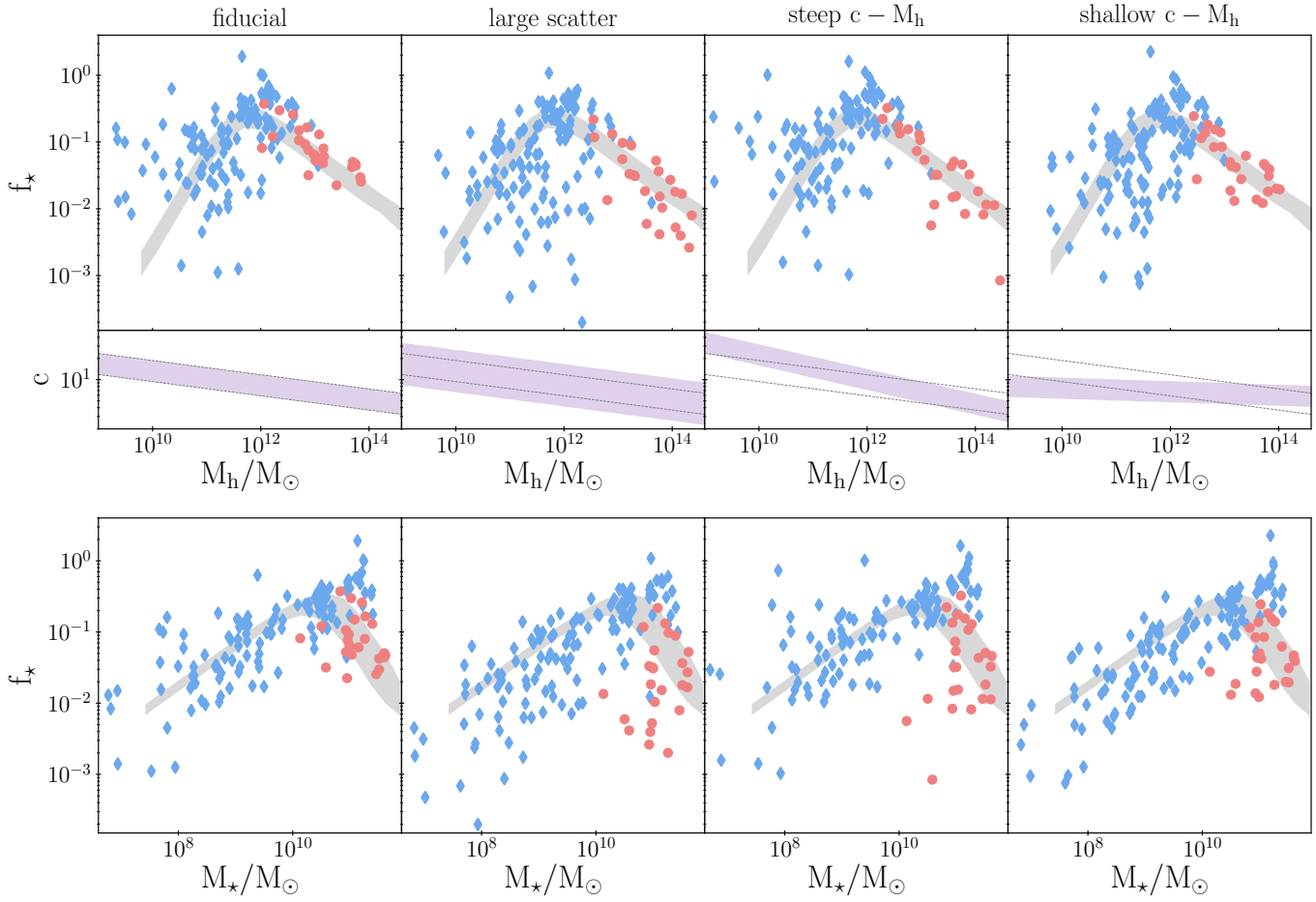

Fig. 5. Effects of varying the prior on the c–$M_{\rm h}$ correlation in our dynamical estimates of the SHMR. *Top (bottom) panels*: resulting $f_\star$–$M_{\rm h}$ ($f_\star$–$M_\star$) relation, where the halo masses of both late types (blue diamonds) and early types (red circles) are calculated with a prior on the c–$M_{\rm h}$ relation that follows the purple shaded area (1σ) in the *middle row* of panels. *From left to right*: the four columns of panels are for the following priors: (i) the fiducial $c - M_{\rm h}$ relation from cosmological simulations by Dutton & Macciò (2014, with slope = −0.101 and scatter = 0.11 dex), (ii) the same $c - M_{\rm h}$ relation but with about twice the scatter (0.25 dex), (iii) a steeper one (slope = −0.2), and (iv) a shallower one (slope = −0.05). The black dashed lines in the *middle panels* show the fiducial c–$M_{\rm h}$ relation for comparison. *Top* and *bottom rows*: the grey shaded area shows the SHMR from Moster et al. (2013) based on abundance matching.

substantially, reaching about 0.34 dex at $M_\star \sim 10^{11}\,M_\odot$[2]. Combining these four dispersions in quadrature, we can nicely explain the observed scatter of 0.4 dex in our estimates of $f_\star$.

Plotting $f_\star$ as a function of $M_{\rm h}$ demonstrates clearly that early types occupy halos of a wide range of masses ($10^{12}\,M_\odot \lesssim M_{\rm h} \lesssim 10^{14}\,M_\odot$). In contrast, late types of similar stellar mass are all found in halos of mass $M_{\rm h} \sim 10^{12}\,M_\odot$, and virtually none occupies halos more massive than $M_{\rm h} \sim 5 \times 10^{12}\,M_\odot$. This is potentially a very important finding since it hints at the existence of an upper limit to the masses of halos within which discs can form (Dekel & Birnboim 2006).

Of all the assumptions in our modelling technique, we found that the prior on the c–$M_{\rm h}$ correlation has the largest effect on estimates of $M_{\rm h}$. In Fig. 5, we show the results of some tests to assess the robustness of our findings. We re-fitted our $f(\boldsymbol{J})$ models to the SLUGGS data with different priors for the halo concentration-mass relation; in particular, we doubled the scatter, and we increased and decreased the slopes of the c–$M_{\rm h}$ relation so as to span the 1σ range of the standard ΛCDM relation over the range of halo masses probed here[3]. These priors are shown in the middle row of panels in Fig. 5. Each column of panels in Fig. 5 shows the $f_\star$–$M_{\rm h}$ (top) and $f_\star$–$M_\star$ (bottom) relations that we obtain when assuming these different priors. To compare early types (red) and late types (blue) consistently, we re-computed the rotation curve decompositions of the late types in SPARC with each prior. From the results plotted in Fig. 5, we note that, while there can be significant differences for individual galaxies, the general trends for the populations of late types and early types remain robust.

These tests give us confidence that the systematic difference between the SHMRs of massive late-type and early-type galaxies is real. An important point that we need to emphasise here is that the c–$M_{\rm h}$ priors that we used for these tests are deliberately extreme. In fact, such a large scatter (0.25 dex) or such steep or shallow slopes are outside the range of published c–$M_{\rm h}$ relations for the standard ΛCDM cosmogony

[2] This happens as a result of the combination of the SHMR with the steeply declining halo mass function. Above the peak, low-mass halos that are high-$f_\star$ outliers of the $f_\star$–$M_{\rm h}$ relation are about as common as high-mass halos with a typical $f_\star$. This not only increases the scatter at a fixed $M_\star$, but it also increases the average $f_\star$ at a fixed $M_\star$ with respect to that obtained by inverting $f_\star(M_{\rm h})$ (see also Moster et al. 2020).

[3] We also repeated this test with systematically larger and smaller concentrations, i.e. with c following the fiducial c–$M_{\rm h}$ relation $\pm 1\sigma$, finding similar results to those shown in Fig. 5.

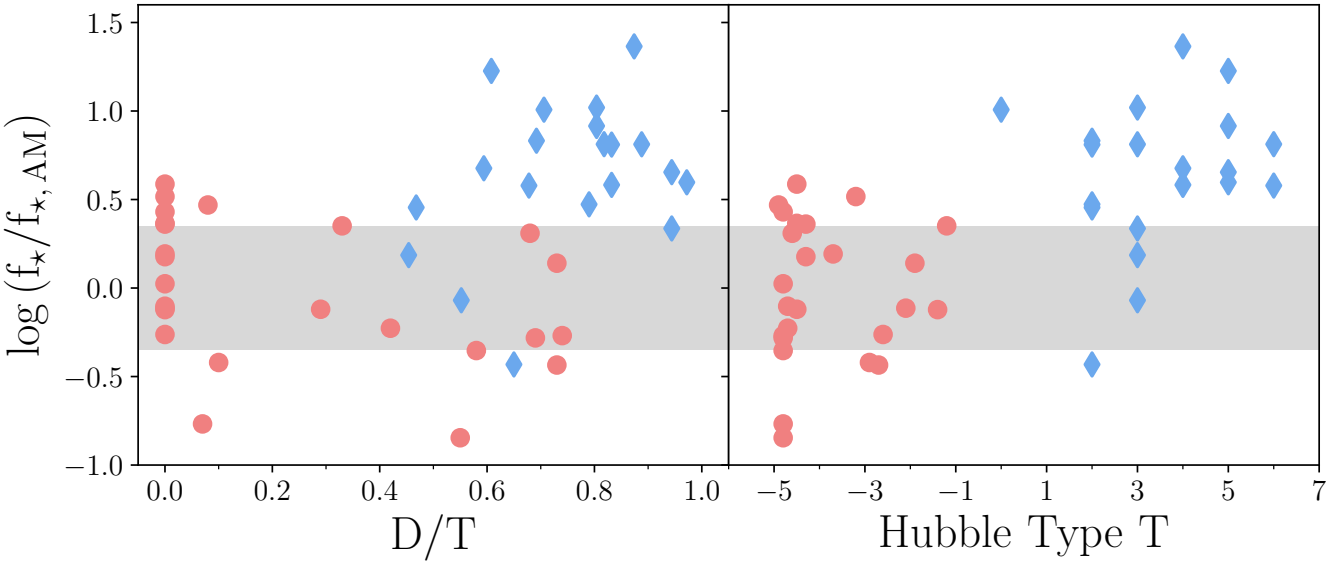

Fig. 6. Residuals of our dynamical estimates of $f_\star$ relative to the abundance-matching values $f_{\star,\mathrm{AM}}$ at the same stellar masses from Moster et al. (2013) versus the disc-to-total ratio D/T (*left*) and Hubble type T (*right*), for massive late types ($M_\star > 5 \times 10^{10}\,M_\odot$, blue diamonds) and early types (red circles). The grey area shows the scatter of the Moster et al. (2013) SHMR near $M_\star \sim 10^{11}\,M_\odot$. Several early types pile up at $D/T = 0$ since no disc component could be clearly identified from their photometry.

(e.g. Diemer & Kravtsov 2015). This allows us to rule out the possibility, with high confidence, that the two branches of the SHMR revealed in Fig. 3 are the result of late types and early types occupying halos with systematically different concentrations. We have also verified this directly from the best-fitting c and M_h values from our models.

3.2. Dependence on disc fraction and morphological type

In Sect. 3.1, we investigated the difference in $f_\star$ between two broadly defined galaxy samples, late types and early types. Here we examine how $f_\star$ depends on disc fraction and morphological type for massive galaxies.

For 21 of the 25 early types in SLUGGS, we rely on the photometric bulge and disc decompositions in the r-band performed by Krajnović et al. (2013), who fitted Sérsic plus exponential functions to the observed 1D photometric profiles. We note that, for half of these, Krajnović et al. (2013) found no significant contribution from an exponential disc component. For the four remaining galaxies, we fitted the 1D R-band profiles from the Carnegie-Irvine Galaxy Survey (Li et al. 2011) with Sérsic plus exponential functions, in order to perform a similar analysis to that of Krajnović et al. (2013).

We include only the 20 late types with the largest stellar masses for this comparison ($M_\star > 5 \times 10^{10}\,M_\odot$). We take the disc-to-total ratios D/T from the *Spitzer* Survey of Stellar Structure in Galaxies (Sheth et al. 2010), based on 2D bulge and disc decompositions of the 3.6 µm *Spitzer* images with the code `galfit` (Peng et al. 2002, 2010), when available. Otherwise, we take them from the kinematic decompositions reported by Fall & Romanowsky (2013, 2018, and references therein). For a few galaxies that do not have D/T from these sources, we use the decomposition of the 1D surface brightness profiles at 3.6 µm performed by Lelli et al. (2016a).

For all of these massive galaxies, we calculate the residual of our estimate of $f_\star$ relative to the abundance-matching value $f_{\star,\mathrm{AM}}$ at the same mass from Moster et al. (2013) and express it in the form $\log(f_\star/f_{\star,\mathrm{AM}})$. We plot this quantity in Fig. 6 as a function of D/T (left) and as a function of the Hubble type T (right), both for late types (blue diamonds) and early types (red circles). We find that bulge-dominated galaxies ($D/T < 0.2$, $T < -3$) have small residuals with respect to abundance matching as they lie within its scatter (grey area). In contrast, disc-dominated galaxies ($D/T > 0.8$, $T > 4$) are found to have systematically larger $f_\star$. The transition between these two regimes occurs at around $D/T \sim 0.5$ or $T \sim 2$. The spirals with lowest disc fractions in this sample ($D/T \sim 0.5$, $T \sim 2$) are indeed in better agreement with abundance matching, although the scatter of the points is substantial. The dependence of $f_\star$ on D/T and on T that we observe in Fig. 6 indicates that the location of a galaxy in the $f_\star$–$M_\star$ diagram depends fairly continuously on its disc fraction and Hubble type.

From this new perspective, we can now see that derivations of the SHMR that include galaxies of all types are likely to overestimate the scatter at the high-mass end. This is because the trend of $f_\star$ with D/T (Fig. 6), if not recognised, will simply be counted as scatter. However, this effect is likely to be small since disc-dominated galaxies are relatively rare at the high-mass end (∼10% at $M_\star \gtrsim 10^{11}\,M_\odot$; Kelvin et al. 2014; Ogle et al. 2019). To gain some intuition on the magnitude of this effect, we performed a simple calculation in an extreme case of a binary population of galaxies: pure discs and pure spheroids. At a fixed $M_\star = 10^{11}\,M_\odot$, we have 90% spheroids on the abundance matching relation, that is, with $f_{\star,\mathrm{AM}}(M_\star)$, and we have 10% discs with $f_\star$ systematically offset from this by a factor of 0.8 dex. In order to match the scatter of the Moster et al. (2013) SHMR at that stellar mass, which is ≈0.35 dex, we need to decrease the intrinsic scatter of the pure spheroid population to ≈0.27 dex. This exercise suggests that calculations that ignore the dependence of the SHMR on morphology will overestimate the intrinsic scatter by about 0.08 dex.

4. Comparison with other estimates of the SHMR

In this section, we compare our derivation of the $f_\star$–$M_\star$ relation for individual late-type and early-type galaxies with other

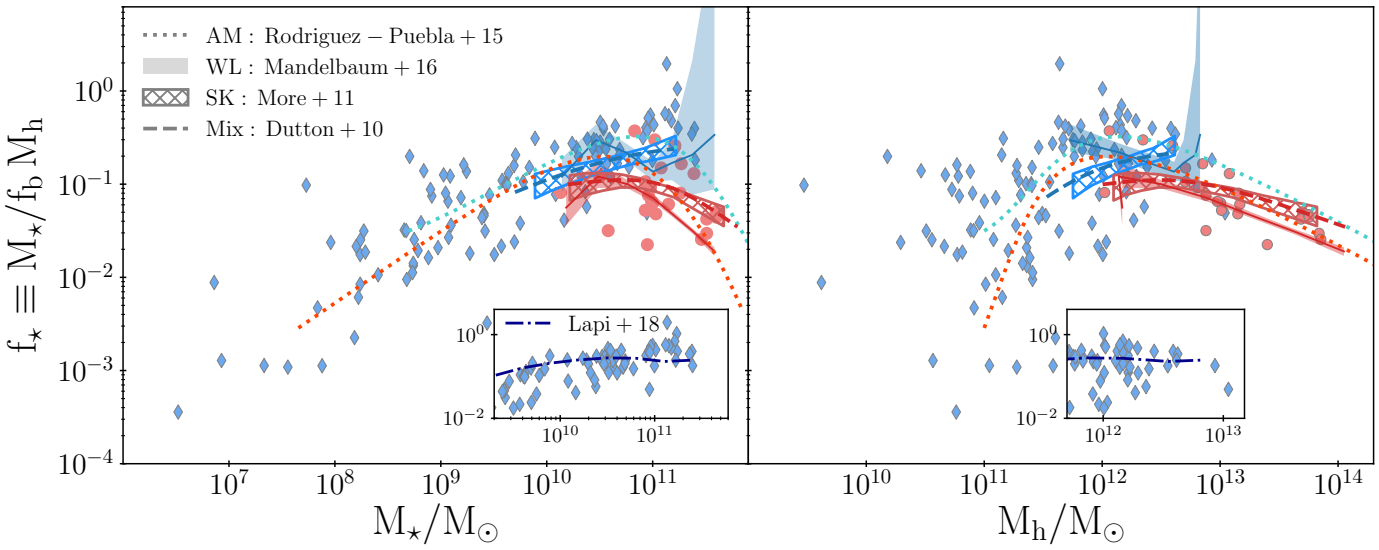

Fig. 7. Same as Fig. 3, but comparing our SHMR with others that are representative of studies based on different techniques: abundance matching (Rodríguez-Puebla et al. 2015), weak lensing (Mandelbaum et al. 2016), satellite kinematics (More et al. 2011), and a combination of thereof (Dutton et al. 2010). Blue colour is used for late types, red colour is used for early types. The insets show the comparison to the estimates of $f_\star$ for late-type galaxies by Lapi et al. (2018). We omit the errorbars here for clarity.

estimates from the literature. Taken together, these results provide additional evidence that galaxies of different types occupy halos of different masses.

4.1. Statistical estimates of the SHMR

In Fig. 7, we show how our SHMR compares to those derived by different techniques, for late (blue) and early types (red) separately. We notice that there is general agreement among these studies, with our SHMR showing perhaps the largest differences between late and early types.

Satellite kinematics (e.g. Conroy et al. 2007; More et al. 2011; Wojtak & Mamon 2013; Lange et al. 2019) and especially weak lensing (e.g. Mandelbaum et al. 2006, 2016; Tinker et al. 2013; Hudson et al. 2015; Taylor et al. 2020) are, in principle, reliable tracers of halo masses out to very large radii. However, these methods rely heavily on stacking hundreds or thousands of galaxies that are usually grouped into late types and early types via a hard cut in colour. These analyses have the advantage of including large numbers of galaxies but the disadvantage that colour is an imperfect proxy for morphology since it depends on a combination of other factors, including star formation rate and history, dust reddening, and metallicity. Hence, the differences between late types and early types will be artificially attenuated. Similar considerations also apply to SHMRs based on empirical models, which are mostly constrained by observed stellar mass functions, with only indirect estimates of halo masses (e.g. Dutton et al. 2010; Rodríguez-Puebla et al. 2015; Behroozi et al. 2019; Moster et al. 2020).

Our work complements these results since it is based on careful estimates of the halo masses of individual galaxies in samples of late types and early types specifically selected for dynamical studies. Our derivation of the SHMR has opposite strengths and weaknesses with respect to the statistical estimates above. It is therefore not surprising that we find a somewhat larger difference in $f_\star$ between late-type and early-type galaxies.

4.2. Individual estimates of halo masses

4.2.1. Early types

The SLUGGS GC data have already been used by Alabi et al. (2016, 2017) to estimate the total halo masses of the galaxies by a simpler method: the so-called tracer mass estimator (TME; Watkins et al. 2010, with original formulation by Bahcall & Tremaine 1981). In this case, the total mass is taken to be $M_{\rm TME} = C\,\hat{R}\hat{V}^2/G$ where G is the gravitational constant, $\hat{R}$ and $\hat{V}$ are a characteristic radius and velocity of the system and C is a dimensionless constant of order unity that is calibrated a priori with some simple assumptions. We compare in Fig. 8 our halo masses with those of Alabi et al. (2017) on a galaxy-by-galaxy basis, finding overall consistency within a factor of a few.

One of the shortcomings of the TME method is that it does not clearly partition between luminous and dark components. This is of particular importance in the context of the SLUGGS early types since the TME is sensitive to the dynamical mass near the median radius of the tracer population ($R_{\rm med,GC}$), which happens to be where the masses of stars and dark matter are comparable (see Fig. 2). Therefore, it is not surprising that the $M_{\rm h}$ estimates of this method are consistent within a factor of a few with those of our $f(\boldsymbol{J})$ models.

Bílek et al. (2019) recently estimated the halo masses of the early-type galaxies in SLUGGS by analysing the kinematics of their GC systems. In particular, they used the GC velocity dispersion profiles together with the Jeans equations to constrain the gravitational potential. They modelled the dark matter halo with a spherical NFW profile, and they imposed a prior on the c–$M_{\rm h}$ relation from cosmological simulations, as in our approach. However, rather than allowing the data to constrain the velocity anisotropy of the GC system, as we do here, they assume a β profile as an input to their model. We compare their estimates of halo masses with ours in Fig. 8. Despite the differences and limitations of their approach, we find that their results are consistent with ours within the uncertainties. This comparison adds to

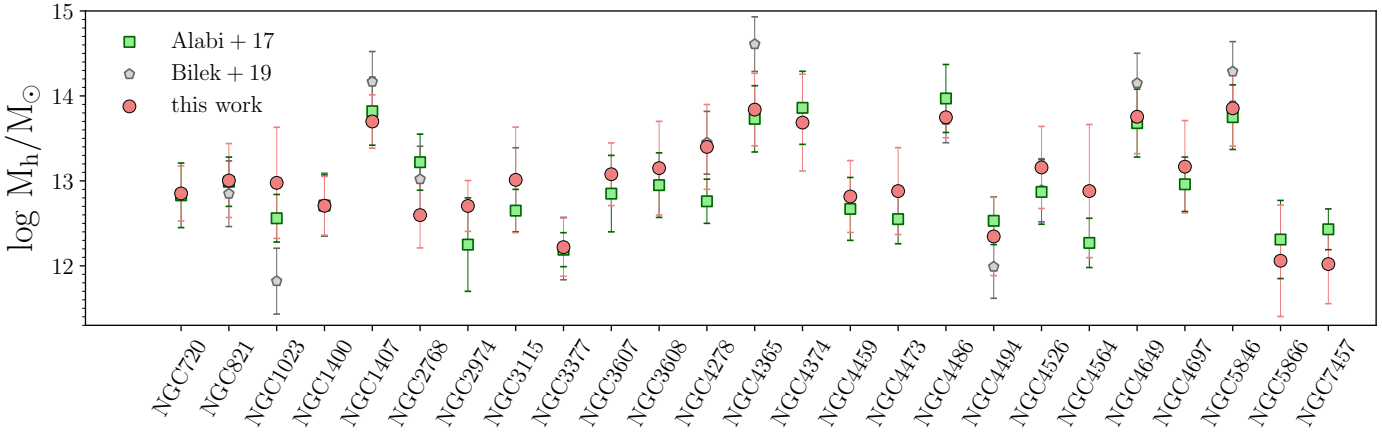

Fig. 8. Comparison of our estimates of halo masses for early-type galaxies in SLUGGS based on $f(\boldsymbol{J})$ models (red circles) with those of Alabi et al. (2017), using the TME (green squares), and those of Bílek et al. (2019), based on a Jeans analysis (grey pentagons).

our confidence that our estimates of M_h are not biased by model-dependent systematic effects.

4.2.2. Late types

Several other studies have derived the SHMR of spiral galaxies from their rotation curves, with results consistent with those from PFM19 shown here in Fig. 3. Lapi et al. (2018) found a similar trend from stacked Hα rotation curves in an independent sample of spirals (see Fig. 7). However, Hα rotation curves typically do not extend as far as HI rotation curves and thus provide only weak constraints on dark matter halo masses (van Albada et al. 1985; Kent 1986, 1987).

Katz et al. (2017) also estimated the halo masses of spiral galaxies in the SPARC sample from HI rotation curve decomposition. However, they either used an unconstrained fit (i.e. with no prior on the c–M_h relation), leaving M_h undetermined, or they imposed a prior on M_h from the Moster et al. (2013) SHMR. While the SHMR they derive naturally follows closely the Moster et al. SHMR by construction, their estimates of M_h are nevertheless in fair agreement with the ones we obtain without imposing a prior on the SHMR. Li et al. (2020) recently revised and expanded their approach to several different types of halo profiles and reached similar conclusions.

It is interesting to notice that a systematic difference between late types and early types was also reported by Tortora et al. (2019) when looking at the dark matter fraction f_DM within one effective radius R_e as a function of stellar mass. They noticed that late types lie on a decreasing f_DM–$M_\star$ relation, while for massive early types this relation inverts, analogous to our results for $1/f_\star$ versus $M_\star$ based on the total masses within the virial radii of the halos. This suggests that, at a fixed $M_\star$, massive discs are less dominated by dark matter than spheroids, both globally and locally (see also Marasco et al. 2020).

4.3. The mass of the GC system as a dark matter halo tracer

Another novel method for estimating dark matter halo masses of galaxies is based on the total mass of their GC system, M_GCS. Several recent studies have demonstrated the existence of a convincing linear relation between M_GCS and M_h for both late types and early types (e.g. Blakeslee et al. 1997; Spitler & Forbes 2009; Georgiev et al. 2010; Harris et al. 2013, 2017; Hudson et al. 2014; Burkert & Forbes 2020). The physical origin of this relation is not well understood (e.g. Kravtsov & Gnedin 2005; Boylan-Kolchin 2017; El-Badry et al. 2019), but we can exploit it as a semi-independent method for deriving the SHMR nonetheless[4]. Thus, we may regard the relation between L_K/M_GCS and L_K as a direct analogue of the $f_\star$–$M_\star$ relation, where L_K is the K-band luminosity. The L_K/M_GCS–L_K relation requires only photometry, rather than spectroscopy of the GCs, making it relatively easy to derive. Harris et al. (2013) have assembled a catalogue of M_GCS for 422 nearby galaxies of all morphological types covering a wide range in luminosities.

We plot in Fig. 9 the ratio L_K/M_GCS as a function of L_K for the galaxies in the Harris et al. (2013) sample, separating them into late types (blue crosses) and early types[5] (orange squares). The similarity between the L_K/M_GCS–L_K relation in Fig. 9 and the $f_\star$–$M_\star$ relation in Fig. 3 is striking; early types turnover at about $L_K \sim 5\times10^{10}\,L_\odot$, while bright late types seem to lie on a separate rising branch (see Kim et al. 2019, for a similar analysis of early types).

The Harris et al. (2013) sample contains 24 out of the 25 SLUGGS early types that we analysed in this work, but only three of the 20 massive spirals in SPARC (NGC 891, NGC 5907, and NGC 7331). The galaxies in common with our detailed analysis are indicated in Fig. 9 by symbols with darker and thicker edges. We notice that the three spirals have systematically higher L_K/M_GCS than any of the early types of similar L_K, in qualitative agreement with what we find on the $f_\star$–$M_\star$ diagram. From this analysis, we conclude that, despite the large scatter, the L_K/M_GCS–L_K relation is quite consistent with our more robust derivation of the $f_\star$–$M_\star$ relation from GC kinematics and HI rotation curves.

5. The SHMR and galaxy scaling laws

In the previous sections, we established that the SHMR of late types and early types follows two distinct branches: one where $f_\star$ increases with mass for spirals, and another one for ellipticals and lenticulars, where $f_\star$ decreases beyond a peak near $M_\star \sim 5\times10^{10}\,M_\odot$. Yet late-type and early-type galaxies are known to

[4] A caveat we note here is that studies that determined the M_GCS–M_h relation often assumed halo masses from a standard SHMR, typically not taking into account the morphology dependence that we highlight in Fig. 3.

[5] Irregulars are excluded from this analysis.

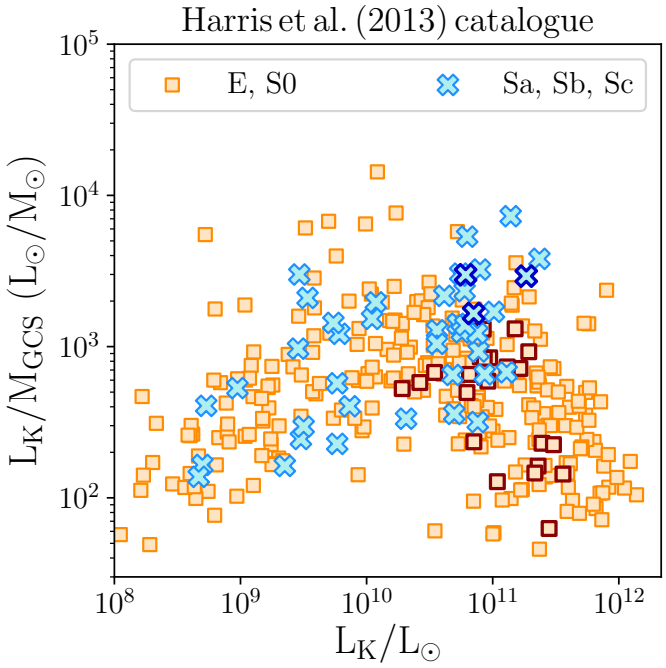

Fig. 9. Ratio of K-band luminosity to the mass of the GC system (L_K/M_{GCS}) versus K-band luminosity for galaxies in the Harris et al. (2013) catalogue. We plot spirals with turquoise crosses, and ellipticals and lenticulars with orange squares. We highlight the galaxies in common between the Harris et al. (2013) catalogue and our work with darker edges.

obey very similar scaling relations between their stellar masses and velocities; the Tully & Fisher (1977) and Faber & Jackson (1976) relations are observed to be pure power laws with no significant features. These two facts may appear to be at odds with each other since velocity is a proxy for dynamical mass, and one might therefore expect the shape of the SHMR to impact the mass-velocity scaling laws (e.g. Ferrero et al. 2017; Posti et al. 2019b).

The resolution of this apparent paradox logically must involve the relations between the characteristic velocities of galaxies and those of their dark matter halos, which need to be different for late types and early types on the two branches of the SHMR. In this section, we demonstrate this difference and discuss its physical implications.

5.1. A paradox and its resolution

We take measurements of the flat parts of HI rotation curves for spirals in SPARC (V_{flat}, Lelli et al. 2016b) and stellar velocity dispersions measured within a fixed radius of 1 kpc for the ellipticals and lenticulars in SLUGGS ($\sigma_{\star,1\,kpc}$, Brodie et al. 2014). These are the two characteristic velocities that we use to define the Tully–Fisher and Faber–Jackson relations, which we compactly write as

$$M_\star \propto V_{gal}^a, \tag{2}$$

where V_{gal} is V_{flat} for late types and $\sigma_{\star,1\,kpc}$ for early types. Along either the rising branch of the SHMR for late types or along the declining one for massive early types, the SHMR can also be approximated by a power law,

$$f_\star \propto M_h^b. \tag{3}$$

Given the definition of $f_\star$ (Eq. (1)) and the fact that, in ΛCDM cosmogonies, halo masses and virial velocities are related by $M_h \propto V_h^3$, we can rearrange the two equations above into a relation between V_{gal} and V_h, which then becomes the power law

$$V_{gal} \propto V_h^c, \tag{4}$$

with

$$c = 3(b+1)/a. \tag{5}$$

Equation (4) is key here since it relates the familiar scaling laws (Eq. (2)) with the two branches of the SHMR (Eq. (3)). With our set of measurements – $M_\star$ from 3.6 μm photometry, V_{gal} from observed HI (V_{flat}) or stellar kinematics ($\sigma_{\star,1\,kpc}$), M_h from dynamical models of rotation curves and GC kinematics – we perform power-law fits to Eqs. (2)–(4), finding

$$a = 4.3 \pm 0.3, \quad b = 0.5 \pm 0.2, \quad c = 1.02 \pm 0.21 \quad \text{(late types)}, \tag{6}$$

$$a = 3.5 \pm 0.7, \quad b = -0.6 \pm 0.1, \quad c = 0.36 \pm 0.17 \quad \text{(early types)}. \tag{7}$$

In Fig. 10, we show (on the top row) the data and the power-law fits of the three relations ($f_\star$–M_h, $M_\star$–V_{gal}, and V_{gal}–V_h) for the late types (blue) and early types (red). While the mass-velocity scaling laws have a similar slope (a), the SHMR and the V_{gal}–V_h relations have significantly different slopes (b and c) on the two branches. At a fixed stellar mass, the large difference in halo mass between discs and spheroids is hidden in the similar Tully–Fisher and Faber–Jackson relations by the different V_{gal}–V_h relations.

The slope $c \approx 1$ for late types on the rising branch of the SHMR means that the ratio V_{flat}/V_h is nearly the same (and about equal to unity) for discs of all masses (Posti et al. 2019b). This is another manifestation of the so-called disc-halo conspiracy, that rotation curves are observed to be flat from the inner, baryon-dominated parts of galactic discs to the outer, dark matter-dominated parts (van Albada et al. 1985; Kent 1986, 1987). On the other hand, for early types along the falling branch of the SHMR, we find a very different result: $c \approx 0.4$, which implies that the ratio $\sigma_{\star,1\,kpc}/V_h$ decreases with both stellar and halo mass.

While V_{flat} for late types is measured at large radii and traces the potential of the dark halo, $\sigma_{\star,1\,kpc}$ for early types is measured in the inner regions where the potential is dominated by stars. One might then wonder whether this is responsible for the difference in the V_{flat}/V_h and $\sigma_{\star,1\,kpc}/V_h$ ratios. We check for this in the bottom panels of Fig. 10, where we replace the observed V_{gal} with the circular velocity evaluated at a fixed radius of $2R_e$ for both late-type and early-type galaxies in our sample. For late types, we obtain the circular velocities directly from the observed rotation curves, while for early types, they are an output of our $f(\boldsymbol{J})$ dynamical models. Figure 10 shows that the difference persists in the relation $V_{circ}(2R_e) \propto V_h^{c'}$. Now we find $c' \approx 1$ for late types and $c' \approx 0.57$ for early types.

5.2. Physical interpretation

The observed scaling relations between the rotation velocities, sizes, and stellar masses of spiral galaxies indicate that they represent a self-similar population of objects homologous to their dark matter halos (e.g. Posti et al. 2019b). In particular, galactic discs have, on average, almost as much specific angular momentum as their dark halos, as expected from simple conservation arguments (Fall & Efstathiou 1980; Dalcanton et al. 1997;

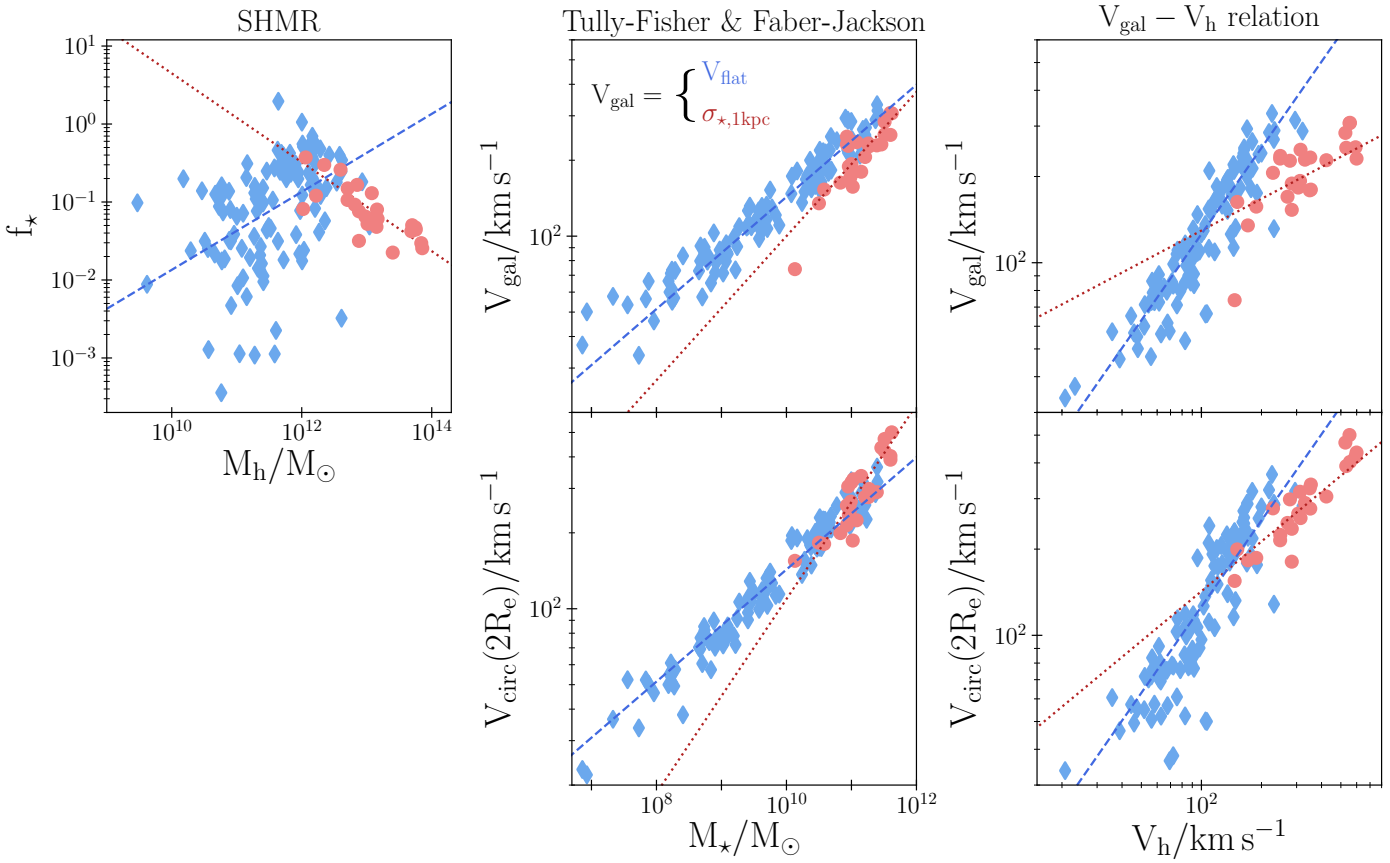

Fig. 10. SHMR ($f_\star - M_h$, *left*), stellar mass-velocity scaling law ($M_\star - V_{gal}$, *middle*), and the relation between galaxy velocity and halo velocity ($V_{gal} - V_h$, *right*) for the population of late types (blue) and massive early types (red). *Top-middle* and *top-right panels*: the characteristic velocity of galaxies V_{gal} is the velocity along the flat parts of HI rotation curves for late types (V_{flat}, Lelli et al. 2016b) and the velocity dispersion of stars within 1 kpc for early types ($\sigma_{\star,1\,kpc}$, Brodie et al. 2014). *Bottom-middle* and *bottom-right panels*: we substitute the observed V_{gal} with the circular velocity evaluated at the same radius ($2R_e$) for both galaxy types. In all panels, we show power-law fits to the data of late types (blue dashed lines) and early types (red dotted lines).

Mo et al. 1998). Stellar feedback modifies this behaviour, making gas retention mass dependent, and thus creating the rising branch of the SHMR. Gravitational clustering and accretion moves galaxies along the scaling laws and up the rising branch of the SHMR. This introduces no features in either the scaling laws or the $f_\star - M_\star$ relation.

However, galaxies in crowded environments, such as groups and clusters, often collide and merge with each other. Depending on the mass ratio of the galaxies and on whether they are gas rich or gas poor, mergers have a couple of important implications for the evolution of massive galaxies. First, the stellar body is dynamically heated, causing the spheroidal component to grow at the expense of the disc component, thus leading to morphological transformation (e.g. Quinn et al. 1993; Hopkins et al. 2010b; Martin et al. 2018). Second, some of the gas in the merging galaxies may be funnelled into the central black hole, thus triggering AGN feedback (e.g. Hopkins et al. 2006). Outflows and radiation from the AGN may then impede further inflow and star formation, hence reducing $f_\star$. As a consequence of merging and AGN feedback, massive discs are driven off the rising branch of the SHMR, becoming passive spheroids on the falling branch.

In the previous subsection, we showed that late types follow a $V_{gal} - V_h$ relation with a slope of $c \approx 1$, implying that the ratio of binding energy per unit mass of the luminous galaxy to that of its dark halo ($\propto V_{gal}^2/V_h^2$) is approximately independent of mass. In contrast, early types have $c \approx 0.4$, indicating that the ratio of galaxy-to-halo binding energy per unit mass decreases as mass increases. Both merging and AGN feedback may reduce the binding energy per unit mass, leading to $c < 1$, as observed.

To understand how mergers can lower the ratio V_{gal}/V_h we consider a typical collision between two galaxies on a weakly bound orbit (Khochfar & Burkert 2006). While the halo mass M_h and the virial velocity V_h increase during merging, idealised simulations have shown that the internal velocity dispersion of the stars typically remains constant or decreases, depending on the mass ratio, gas fraction, and orbital parameters (e.g. Nipoti et al. 2003; Cox et al. 2006; Naab et al. 2009; Hilz et al. 2012; Posti et al. 2014). After some Gyr of evolution in a dense environment, a massive early type that experiences several mergers will therefore lower its V_{gal}/V_h ratio as its mass increases. This effect is also observed in cosmological simulations, where frequent minor mergers deposit stars primarily in the outskirts of massive galaxies, thus lowering their binding energy per unit mass (e.g. Oser et al. 2012; Gabor & Davé 2012).

At the same time, outflows launched by the AGN will interact with the circumgalactic medium, pushing some of it outwards, depending on the opening angle of the outflow. If this gas is ever able to condense and form stars, this would also tend to lower the binding energy per unit mass of the host galaxy.

Mergers and AGN feedback may thus combine to transform star-forming discs on the rising branch of the SHMR into quenched spheroids on the falling branch. These two processes

are contemporaneous but episodic. Both mergers and AGN feedback tend to disrupt inflow onto galactic discs, thus suppressing disc growth while promoting spheroid growth. Between these episodes, relatively smooth inflow can resume, thus promoting the regrowth of discs. This reasoning suggests that massive galaxies may evolve along complicated, essentially stochastic, paths in the region of the $f_\star - M_\star$ diagram bounded by the rising pure-disc branch and the declining pure-spheroid branch.

6. Summary and conclusions

In this paper, we have derived the SHMR for a sample of 25 massive early-type galaxies from estimates of their individual halo masses. We accomplished this by comparing a dynamical model with a flexible analytical distribution function with position and velocity data for the GC systems around these galaxies. Combining our new results for early types with those from PFM19 for late types based on extended HI rotation curves, we derived, for the first time, the $f_\star - M_\star$ relation for galaxies of different morphologies with identical assumptions about their halo properties. Our main findings can be summarised as follows.

(i) At the high-mass end of the SHMR ($M_\star > 5 \times 10^{10}\,M_\odot$), late types are found to have significantly higher $f_\star$ than early types of the same stellar mass (by a factor of $\sim$7 at $M_\star \sim 10^{11}\,M_\odot$). While $f_\star$ increases with $M_\star$ for late types (PFM19), it decreases for early types, in broad agreement with expectations from abundance matching (e.g. Moster et al. 2013). Our results show unequivocally that the SHMR has a secondary correlation with galaxy type at the high-mass end.

(ii) For massive galaxies ($M_\star > 5 \times 10^{10}\,M_\odot$), we studied how $f_\star$ deviates from the expectations of abundance matching ($f_{\star,\mathrm{AM}}$) as a function of disc fraction and Hubble type. We find a fairly continuous transition between close agreement, $\log(f_\star/f_{\star,\mathrm{AM}}) \sim 0$, for pure spheroids, and an order of magnitude difference, $\log(f_\star/f_{\star,\mathrm{AM}}) \sim 1$, for pure discs. This transition occurs at about $D/T \sim 0.5$, or $T \sim 2$, suggestive of scenarios involving merging and AGN feedback.

(iii) We have tested the sensitivity of our M_h estimates with respect to our adopted priors on the $c - M_\mathrm{h}$ correlation. We find that the secondary correlation of the SHMR with galaxy type is robust relative to any reasonable adjustments to this prior. We have also compared our results both with other statistical derivations of the SHMR (e.g. using weak lensing or satellite kinematics) and with other individual estimates of halo masses based on different data and/or techniques. We find these estimates to be compatible within the uncertainties, allowing us to conclude that the issue of whether the SHMR has a secondary correlation with galaxy type is now settled.

(iv) We investigated the apparent paradox between the two separate branches of the SHMR – a rising one for discs and a falling one for massive spheroids – and the similar power-law relations between stellar masses and velocities for late types and early types, the Tully–Fisher and Faber–Jackson relations. We demonstrated that this happens because the relations between galaxy velocity and halo velocity are different for galaxies of different types. Discs have a constant ratio $V_\mathrm{gal}/V_\mathrm{h} \approx 1$ at all masses – indicating that they are close to homologous with their dark halos – while spheroids have a declining ratio $V_\mathrm{gal}/V_\mathrm{h}$ with mass. We suggest that this is a signature of the combined effects of merging and AGN feedback.

As suggested above, both merging and AGN feedback are likely responsible for splitting the SHMR and the $V_\mathrm{gal} - V_\mathrm{h}$ relation into different branches for discs and spheroids, but their exact roles remain to be determined. The growth of discs and spheroids in massive galaxies may be intermittent, with disc growth during periods of relatively smooth inflow, interrupted by spheroid growth during episodes of merging and AGN feedback. Hydrodynamical simulations may shed light on the underlying physical processes, so long as they are relatively insensitive to numerical resolution and subgrid recipes for stellar and AGN feedback. A careful census of black holes in a large sample of host galaxies of different morphologies and masses likely would also be instructive.

Acknowledgements. We thank Michal Bílek, Benoit Famaey, and Filippo Fraternali for encouragement in the early stages of this project and Romeel Davé, Ken Freeman, and Andrey Kravtsov for helpful comments in the later stages. LP acknowledges support from the Centre National d'Etudes Spatiales (CNES). This research has made use of "Aladin sky atlas" developed at CDS, Strasbourg Observatory, France (Bonnarel et al. 2000).

References

Alabi, A. B., Forbes, D. A., Romanowsky, A. J., et al. 2016, MNRAS, 460, 3838
Alabi, A. B., Forbes, D. A., Romanowsky, A. J., et al. 2017, MNRAS, 468, 3949
Arnold, V. I. 1978, Mathematical Methods of Classical Mechanics (New York: Springer)
Bahcall, J. N., & Tremaine, S. 1981, ApJ, 244, 805
Behroozi, P. S., Wechsler, R. H., & Conroy, C. 2013, ApJ, 770, 57
Behroozi, P., Wechsler, R. H., Hearin, A. P., & Conroy, C. 2019, MNRAS, 488, 3143
Bílek, M., Samurović, S., & Renaud, F. 2019, A&A, 625, A32
Binney, J. 2010, MNRAS, 401, 2318
Binney, J. 2014, MNRAS, 440, 787
Binney, J., & Tremaine, S. 2008, Galactic Dynamics: Second Edition (Princeton: Princeton University Press)
Binney, J., & Wong, L. K. 2017, MNRAS, 467, 2446
Blakeslee, J. P., Tonry, J. L., & Metzger, M. R. 1997, AJ, 114, 482
Bonnarel, F., Fernique, P., Bienaymé, O., et al. 2000, A&AS, 143, 33
Born, M. 1927, The Mechanics of the Atom (London: G. Bell and Sons, Ltd.)
Boylan-Kolchin, M. 2017, MNRAS, 472, 3120
Brodie, J. P., Romanowsky, A. J., Strader, J., et al. 2014, ApJ, 796, 52
Burkert, A., & Forbes, D. A. 2020, AJ, 159, 56
Conroy, C., Wechsler, R. H., & Kravtsov, A. V. 2006, ApJ, 647, 201
Conroy, C., Prada, F., Newman, J. A., et al. 2007, ApJ, 654, 153
Correa, C. A., & Schaye, J. 2020, MNRAS, 499, 3578
Cox, T. J., Dutta, S. N., Di Matteo, T., et al. 2006, ApJ, 650, 791
Croton, D. J., Springel, V., White, S. D. M., et al. 2006, MNRAS, 365, 11
Dalcanton, J. J., Spergel, D. N., & Summers, F. J. 1997, ApJ, 482, 659
de Blok, W. J. G., McGaugh, S. S., Bosma, A., & Rubin, V. C. 2001, ApJ, 552, L23
de Blok, W. J. G., Walter, F., Brinks, E., et al. 2008, AJ, 136, 2648
Dekel, A., & Birnboim, Y. 2006, MNRAS, 368, 2
Dekel, A., & Silk, J. 1986, ApJ, 303, 39
Diemer, B., & Kravtsov, A. V. 2015, ApJ, 799, 108
Dutton, A. A., & Macciò, A. V. 2014, MNRAS, 441, 3359
Dutton, A. A., Conroy, C., van den Bosch, F. C., Prada, F., & More, S. 2010, MNRAS, 407, 2
El-Badry, K., Quataert, E., Weisz, D. R., Choksi, N., & Boylan-Kolchin, M. 2019, MNRAS, 482, 4528
Faber, S. M., & Jackson, R. E. 1976, ApJ, 204, 668
Fabian, A. C. 2012, ARA&A, 50, 455
Fall, S. M., & Efstathiou, G. 1980, MNRAS, 193, 189
Fall, S. M., & Romanowsky, A. J. 2013, ApJ, 769, L26
Fall, S. M., & Romanowsky, A. J. 2018, ApJ, 868, 133
Ferrero, I., Navarro, J. F., Abadi, M. G., et al. 2017, MNRAS, 464, 4736
Forbes, D. A., Alabi, A., Brodie, J. P., et al. 2017a, AJ, 153, 114
Forbes, D. A., Sinpetru, L., Savorgnan, G., et al. 2017b, MNRAS, 464, 4611
Foreman-Mackey, D., Hogg, D. W., Lang, D., & Goodman, J. 2013, PASP, 125, 306
Foster, C., Pastorello, N., Roediger, J., et al. 2016, MNRAS, 457, 147
Gabor, J. M., & Davé, R. 2012, MNRAS, 427, 1816
Georgiev, I. Y., Puzia, T. H., Goudfrooij, P., & Hilker, M. 2010, MNRAS, 406, 1967

Grand, R. J. J., van de Voort, F., Zjupa, J., et al. 2019, MNRAS, 490, 4786
Harris, W. E., Harris, G. L. H., & Alessi, M. 2013, ApJ, 772, 82
Harris, W. E., Blakeslee, J. P., & Harris, G. L. H. 2017, ApJ, 836, 67
Harrison, C. M. 2017, Nat. Astron., 1, 0165
Hearin, A. P., Watson, D. F., Becker, M. R., et al. 2014, MNRAS, 444, 729
Hilz, M., Naab, T., Ostriker, J. P., et al. 2012, MNRAS, 425, 3119
Hopkins, P. F., Hernquist, L., Cox, T. J., et al. 2006, ApJS, 163, 1
Hopkins, P. F., Croton, D., Bundy, K., et al. 2010a, ApJ, 724, 915
Hopkins, P. F., Bundy, K., Croton, D., et al. 2010b, ApJ, 715, 202
Hudson, M. J., Harris, G. L., & Harris, W. E. 2014, ApJ, 787, L5
Hudson, M. J., Gillis, B. R., Coupon, J., et al. 2015, MNRAS, 447, 298
Jeans, J. H. 1915, MNRAS, 76, 70
Katz, H., Lelli, F., McGaugh, S. S., et al. 2017, MNRAS, 466, 1648
Kelvin, L. S., Driver, S. P., Robotham, A. S. G., et al. 2014, MNRAS, 444, 1647
Kent, S. M. 1986, AJ, 91, 1301
Kent, S. M. 1987, AJ, 93, 816
Khochfar, S., & Burkert, A. 2006, A&A, 445, 403
Kim, D.-W., James, N., Fabbiano, G., Forbes, D., & Alabi, A. 2019, MNRAS, 488, 1072
King, A., & Pounds, K. 2015, ARA&A, 53, 115
Kormendy, J., & Ho, L. C. 2013, ARA&A, 51, 511
Krajnović, D., Alatalo, K., Blitz, L., et al. 2013, MNRAS, 432, 1768
Kravtsov, A. V., & Gnedin, O. Y. 2005, ApJ, 623, 650
Kravtsov, A. V., Berlind, A. A., Wechsler, R. H., et al. 2004, ApJ, 609, 35
Kravtsov, A. V., Vikhlinin, A. A., & Meshcheryakov, A. V. 2018, Astron. Lett., 44, 8
Lange, J. U., van den Bosch, F. C., Zentner, A. R., Wang, K., & Villarreal, A. S. 2019, MNRAS, 487, 3112
Lapi, A., Salucci, P., & Danese, L. 2018, ApJ, 859, 2
Leauthaud, A., Tinker, J., Bundy, K., et al. 2012, ApJ, 744, 159
Lelli, F., McGaugh, S. S., & Schombert, J. M. 2016a, AJ, 152, 157
Lelli, F., McGaugh, S. S., & Schombert, J. M. 2016b, ApJ, 816, L14
Li, Z.-Y., Ho, L. C., Barth, A. J., & Peng, C. Y. 2011, ApJS, 197, 22
Li, P., Lelli, F., McGaugh, S., & Schombert, J. 2020, ApJS, 247, 31
Lynden-Bell, D. 1962, MNRAS, 124, 1
Mandelbaum, R., Seljak, U., Kauffmann, G., Hirata, C. M., & Brinkmann, J. 2006, MNRAS, 368, 715
Mandelbaum, R., Wang, W., Zu, Y., et al. 2016, MNRAS, 457, 3200
Marasco, A., Posti, L., Oman, K., et al. 2020, A&A, 640, A70
Martin, G., Kaviraj, S., Devriendt, J. E. G., Dubois, Y., & Pichon, C. 2018, MNRAS, 480, 2266
Martinsson, T. P. K., Verheijen, M. A. W., Westfall, K. B., et al. 2013, A&A, 557, A131
Mo, H. J., Mao, S., & White, S. D. M. 1998, MNRAS, 295, 319
More, S., van den Bosch, F. C., Cacciato, M., et al. 2011, MNRAS, 410, 210
Moster, B. P., Naab, T., & White, S. D. M. 2013, MNRAS, 428, 3121
Moster, B. P., Naab, T., & White, S. D. M. 2018, MNRAS, 477, 1822
Moster, B. P., Naab, T., & White, S. D. M. 2020, MNRAS, 499, 4748
Naab, T., Johansson, P. H., & Ostriker, J. P. 2009, ApJ, 699, L178
Navarro, J. F., Frenk, C. S., & White, S. D. M. 1996, ApJ, 462, 563
Nipoti, C., Londrillo, P., & Ciotti, L. 2003, MNRAS, 342, 501
Ogle, P. M., Lanz, L., Appleton, P. N., Helou, G., & Mazzarella, J. 2019, ApJS, 243, 14
Oh, S.-H., de Blok, W. J. G., Brinks, E., Walter, F., & Kennicutt, R. C., Jr. 2011, AJ, 141, 193
Oser, L., Naab, T., Ostriker, J. P., & Johansson, P. H. 2012, ApJ, 744, 63
Pascale, R., Posti, L., Nipoti, C., & Binney, J. 2018, MNRAS, 480, 927
Peacock, J. A., & Smith, R. E. 2000, MNRAS, 318, 1144
Peng, C. Y., Ho, L. C., Impey, C. D., & Rix, H.-W. 2002, AJ, 124, 266
Peng, Y.-J., Lilly, S. J., Kovač, K., et al. 2010, ApJ, 721, 193
Planck Collaboration VI. 2020, A&A, 641, A6
Posti, L., & Helmi, A. 2019, A&A, 621, A56
Posti, L., Nipoti, C., Stiavelli, M., & Ciotti, L. 2014, MNRAS, 440, 610
Posti, L., Binney, J., Nipoti, C., & Ciotti, L. 2015, MNRAS, 447, 3060
Posti, L., Fraternali, F., & Marasco, A. 2019a, A&A, 626, A56 (PFM19)
Posti, L., Marasco, A., Fraternali, F., & Famaey, B. 2019b, A&A, 629, A59
Pota, V., Romanowsky, A. J., Brodie, J. P., et al. 2015, MNRAS, 450, 3345
Pulsoni, C., Gerhard, O., Arnaboldi, M., et al. 2018, A&A, 618, A94
Quinn, P. J., Hernquist, L., & Fullagar, D. P. 1993, ApJ, 403, 74
Reddick, R. M., Wechsler, R. H., Tinker, J. L., & Behroozi, P. S. 2013, ApJ, 771, 30
Rodríguez-Puebla, A., Avila-Reese, V., Yang, X., et al. 2015, ApJ, 799, 130
Rodríguez-Puebla, A., Primack, J. R., Avila-Reese, V., & Faber, S. M. 2017, MNRAS, 470, 651
Saito, S., Leauthaud, A., Hearin, A. P., et al. 2016, MNRAS, 460, 1457
Sanders, J. L., & Binney, J. 2016, MNRAS, 457, 2107
Sanders, J. L., & Evans, N. W. 2015, MNRAS, 454, 299
Sersic, J. L. 1968, Atlas de Galaxias Australes (Cordoba, Argentina: Observatorio Astronomico)
Sheth, K., Regan, M., Hinz, J. L., et al. 2010, PASP, 122, 1397
Spitler, L. R., & Forbes, D. A. 2009, MNRAS, 392, L1
Taylor, E. N., Cluver, M. E., Duffy, A., et al. 2020, MNRAS, 499, 2896
Tinker, J., Kravtsov, A. V., Klypin, A., et al. 2008, ApJ, 688, 709
Tinker, J. L., Leauthaud, A., Bundy, K., et al. 2013, ApJ, 778, 93
Tinker, J. L., Brownstein, J. R., Guo, H., et al. 2017, ApJ, 839, 121
Tortora, C., Posti, L., Koopmans, L. V. E., & Napolitano, N. R. 2019, MNRAS, 489, 5483
Tully, R. B., & Fisher, J. R. 1977, A&A, 54, 661
Tumlinson, J., Peeples, M. S., & Werk, J. K. 2017, ARA&A, 55, 389
Vale, A., & Ostriker, J. P. 2004, MNRAS, 353, 189
van Albada, T. S., Bahcall, J. N., Begeman, K., & Sancisi, R. 1985, ApJ, 295, 305
van Uitert, E., Cacciato, M., Hoekstra, H., et al. 2016, MNRAS, 459, 3251
Vasiliev, E. 2019, MNRAS, 482, 1525
Veilleux, S., Cecil, G., & Bland-Hawthorn, J. 2005, ARA&A, 43, 769
Watkins, L. L., Evans, N. W., & An, J. H. 2010, MNRAS, 406, 264
Wechsler, R. H., & Tinker, J. L. 2018, ARA&A, 56, 435
Williams, A. A., & Evans, N. W. 2015, MNRAS, 448, 1360
Williams, A. A., Evans, N. W., & Bowden, A. D. 2014, MNRAS, 442, 1405
Wojtak, R., & Mamon, G. A. 2013, MNRAS, 428, 2407
Yang, X., Mo, H. J., & van den Bosch, F. C. 2008, ApJ, 676, 248
Zhao, H. 1996, MNRAS, 278, 488
Zheng, Z., Coil, A. L., & Zehavi, I. 2007, ApJ, 667, 760
Zu, Y., & Mandelbaum, R. 2015, MNRAS, 454, 1161

Appendix A: Action-based dynamical models of early-type galaxies

Here, we describe the dynamical models that we use to represent the distribution function of GC systems around 25 ellipticals and lenticulars and their dark matter halos. We first summarise the basic principles of models based on action-angle variables, and then we describe our application to the study of early types. For a more complete introduction to action-angle variables, we refer the reader to the monographs by Born (1927) and Arnold (1978). We use the code `AGAMA` (Vasiliev 2019) to evaluate actions, potentials, and distribution functions, and to generate the dynamical models in this work.

A.1. Preliminaries

We begin with the distribution function (DF) for a GC system f, defined such that $f(\boldsymbol{x},\boldsymbol{v})\mathrm{d}\boldsymbol{x}\mathrm{d}\boldsymbol{v}$ is the probability of finding a cluster in the infinitesimal volume element $\mathrm{d}\boldsymbol{x}\mathrm{d}\boldsymbol{v}$ at the position-velocity point $(\boldsymbol{x},\boldsymbol{v})$ in phase space. According to the strong form of the Jeans (1915) theorem, in a steady state, f is a function of the integrals of motion (see also Lynden-Bell 1962). Without loss of generality, we may choose these to be the three actions

$$J_i = \frac{1}{2\pi}\oint p_i \mathrm{d}q_i \quad \text{for } i = 1,2,3, \tag{A.1}$$

where p_i and q_i are canonically conjugate momenta and coordinates, and we write the DF as $f(\boldsymbol{J})$.

Actions $\boldsymbol{J}$ and their canonically conjugate angles $\boldsymbol{\theta}$ are the 'natural' coordinates of galactic dynamics, since (i) the description of orbits becomes mathematically simplest, (ii) they describe systems both in and out of equilibrium, and (iii) actions are adiabatic invariants, that is, they are constant under slow changes of the potential (see Binney & Tremaine 2008). $f(\boldsymbol{J})$ models have been somewhat underused in galactic dynamics, mainly because actions generally cannot be expressed with algebraic functions of positions and velocities and need to be computed numerically. In recent years, several crucial advances have made it feasible to calculate $\boldsymbol{J}$ efficiently in arbitrary potentials (see e.g. Sanders & Binney 2016, and references therein). This, in turn, has led to the introduction of several analytic $f(\boldsymbol{J})$ DFs tailored to model different galaxy components (Binney 2010; Posti et al. 2015; Sanders & Evans 2015; Pascale et al. 2018; Vasiliev 2019).

In this work, we deal mostly with spherical potentials, which greatly simplifies the numerical calculations. In the case of a spherical system, the motion of each particle is confined to a plane, whose orbit can be characterised by two actions. One of these is the total angular momentum, $L = |\boldsymbol{L}|$, and the other is the radial action

$$J_\mathrm{r} = \frac{1}{\pi}\int_{r_\mathrm{apo}}^{r_\mathrm{peri}} p_\mathrm{r}\mathrm{d}r = \frac{1}{\pi}\int_{r_\mathrm{apo}}^{r_\mathrm{peri}} \left(2E - 2\Phi - L^2/r\right)^{1/2}\mathrm{d}r, \tag{A.2}$$

where p_r and r are the radial momentum and position, $E = p_\mathrm{r}^2/2 + L^2/2r^2 + \Phi$ is the energy, Φ is the gravitational potential, and r_apo and r_peri are the apocentre and pericentre of the orbit. Thus, in the spherical case, we have $\boldsymbol{J} = (J_\mathrm{r}, L)$ and $f(\boldsymbol{J}) = f(J_\mathrm{r}, L)$.

A.2. Distribution function

To describe the phase-space distribution of GCs, we use the DF introduced by Posti et al. (2015, see also Williams & Evans 2015; Vasiliev 2019). This is

$$f(\boldsymbol{J}) = \frac{M_0}{(2\pi J_0)^3}\left[1+\left(\frac{J_0}{h(\boldsymbol{J})}\right)^A\right]^{\Gamma/A}\left[1+\left(\frac{g(\boldsymbol{J})}{J_0}\right)^A\right]^{(B-\Gamma)/A}, \tag{A.3}$$

where

$$h(\boldsymbol{J}) = \nu_h J_\mathrm{r} + \frac{3-\nu_h}{2}L,$$
$$g(\boldsymbol{J}) = \nu_g J_\mathrm{r} + \frac{3-\nu_g}{2}L. \tag{A.4}$$

Here, M_0 is a parameter proportional to the mass of the system described by the DF; since we are treating the GCs as tracers of the potential, M_0 is unimportant in this context. The DF of Eq. (A.3) has six free parameters, all with specific physical meanings. The parameters Γ and B control the asymptotic slopes of the density profile in the inner ($r \to 0$) and outer parts ($r \to \infty$), respectively, while the parameter A controls the sharpness of the transition between these regimes. In the case $A = 1$, the two slopes Γ and B have a direct correspondence to the asymptotic slopes of the density distribution[6]. J_0 is a characteristic action that defines the radial scale at which the transition between the two regimes occurs. The last two parameters, ν_h and ν_g, control the velocity anisotropy of the model in the inner and outer parts, respectively.

An important advantage of the double power-law $f(\boldsymbol{J})$ in Eq. (A.3), over models that depend on (E, L), is that in the former case the density distribution effectively decouples from the velocity distribution. This allows us to fix at the outset the parameters of the DF that regulate the density profile of a GC system (A, B, Γ) and then to fit only for those that determine the velocity anisotropy of the system (J_0, ν_h, ν_g). Such decoupling is possible because, for double power-law models, the homogeneous functions $h(\boldsymbol{J})$ and $g(\boldsymbol{J})$ are designed to approximate surfaces of constant energy in action space (Williams et al. 2014; Posti et al. 2015). Thus, h and g largely determine the differential energy distribution $\mathrm{d}N/\mathrm{d}E$ and hence the density profile of the model (see Sect. 4.3 in Binney & Tremaine 2008). Starting from a quasi-ergodic model, where J_r and L appear on an equal footing in h and g, one can easily make the model anisotropic by varying ν_h and ν_g without altering the radial density profile (Binney 2014; Posti et al. 2015).

As a first step in our modelling procedure, we fix the two slopes Γ and B and the sharpness A by matching to the observed number density profile of GCs. In Fig. 1b, we show this fit for the GC system of the galaxy NGC 4494, with $(A, B, \Gamma) = (2.1, 5.3, 0.9)$. We find that, in all cases, the double power-law density profiles generated by Eq. (A.3) provide a very good description of the observed GC number density profiles. The remaining three parameters, J_0, ν_h and ν_g, are instead allowed to vary, but, for internal consistency of the DF, we need to require $0 < \nu_h, \nu_g < 3$ (see Posti et al. 2015; Vasiliev 2019).

A.3. Gravitational potential

We model the mass distribution of each galaxy with two spherical components; the stellar body of the galaxy and its dark matter halo – the GC system is then regarded as a tracer with negligible mass. The stellar distribution is described by a numerically

[6] Posti et al. (2015) showed that a self-consistent model with DF as in Eq. (A.3) and $A = 1$ generates a density law that is very similar to that of a $\alpha\beta\gamma$-model (Zhao 1996) with $\alpha = 1$, $\Gamma = (6-\gamma)/(4-\gamma)$, and $B = 2\beta - 3$.

deprojected Sersic (1968) profile derived from the photometry of 3.6 µm *Spitzer* images by Forbes et al. (2017b). We fix all the parameters of the stellar component, except its mass-to-light ratio at 3.6 µm, which we allow to vary with a log-normal prior with a central value estimated by Forbes et al. (2017b) from stellar population models, and a dispersion of 0.2 dex.

The dark matter halo in our model is described by a standard NFW profile. This has two free parameters: the virial mass (M_h) and concentration (c), which we allow to vary. While we adopt a flat (uninformative) prior on the halo mass, we use a prior for the concentration that follows the mean $c{-}M_\mathrm{h}$ correlation from ΛCDM simulations, with a scatter of 0.11 dex (Dutton & Macciò 2014). Thus, overall our models have six free parameters: three for the potential and three for the DF.

Several of our galaxies appear flattened on the sky, so it is important to determine whether the assumption of spherical symmetry for the stellar component of the potential significantly affects our results. To check this, we re-ran all of our models with an axisymmetric galaxy mass distribution that has the same 3D flattening as the 2D image (Forbes et al. 2017b), while the dark matter halo is still spherical. With respect a spherical galaxy with the same mass, the deviations in the resulting halo masses are always well within the uncertainties[7]. We are therefore confident that the assumption of spherical symmetry in the galactic mass distribution does not significantly bias our results.

A.4. Parameter estimation

We estimate the posterior distributions of the model parameters ($\boldsymbol{\varpi}$) with standard Bayesian inference: $P(\boldsymbol{\varpi}|\boldsymbol{d}) \propto P(\boldsymbol{d}|\boldsymbol{\varpi})\,P(\boldsymbol{\varpi})$, where $\boldsymbol{d}$ are the data, $P(\boldsymbol{d}|\boldsymbol{\varpi})$ is the likelihood, and $P(\boldsymbol{\varpi})$ is the prior. We adopt a prior that is flat (uninformative) for four parameters ($\log M_\mathrm{h}$, $\log J_0$, ν_h, and ν_g), Gaussian for $\log M/L_{3.6}$, with a mean estimated for each galaxy by Forbes et al. (2017b) from stellar population models and a dispersion of 0.2 dex, and Gaussian for $\log c$, with a mean given by the ΛCDM relation and a dispersion of 0.11 dex.

The DF in Eq. (A.3) itself is a probability distribution that can serve as the likelihood in our framework. Specifically, for a set of N particles with position-velocity coordinates (x_i, v_i) orbiting in a given potential Φ, the likelihood, given the model $f(\boldsymbol{J})$, is simply $\prod_{i=0}^{N} f[\boldsymbol{J}(x_i, v_i)]$. In reality, when dealing with data, one does not know the positions and velocities with infinite precision; thus, a convolution of the DF with the observed error distribution is needed (see Binney & Wong 2017; Posti & Helmi 2019).

In our case, we also lack information about the two transverse velocities and the precise positions of the GCs along the LOS. To take this into account, we marginalise the likelihood over all of the realistically possible transverse velocities and LOS positions of the clusters. For the two unknown transverse velocities (v_x, v_y), we adopt uniform distributions in the range $[-V_\mathrm{esc}, V_\mathrm{esc}]$, where V_esc is the escape velocity of the potential. For the unknown LOS position z, we adopt the deprojected density distribution of the GC system $\rho(s)$, where s is the spherical radius, $s^2 = x_\mathrm{GC}^2 + y_\mathrm{GC}^2 + z^2$, evaluated at a fixed position on the sky $(x_\mathrm{GC}, y_\mathrm{GC})$. Thus, we have the following error distribution

$$\mathcal{E}(\boldsymbol{u}|\boldsymbol{d}) = \delta(x - x_\mathrm{GC})\,\delta(y - y_\mathrm{GC})\,G(v_z|V_\mathrm{los}, \epsilon_{V_\mathrm{los}}) \times \rho(z)\,U(v_x| - V_\mathrm{esc}, V_\mathrm{esc})\,U(v_y| - V_\mathrm{esc}, V_\mathrm{esc}), \quad (A.5)$$

where $\boldsymbol{u} = (x, y, z, v_x, v_y, v_z)$ is a point in phase space in a Cartesian frame centred on the galaxy, and $\boldsymbol{d} = (x_\mathrm{GC}, y_\mathrm{GC}, V_\mathrm{los}, \epsilon_{V_\mathrm{los}})$ are the observations. Here ρ is the deprojected density distribution derived from the observed GC number counts profile (Fig. 1b), $G(v_z|V_\mathrm{los}, \epsilon_{V_\mathrm{los}})$ is a Gaussian distribution with mean V_los and dispersion $\epsilon_{V_\mathrm{los}}$, $U(v| - V_\mathrm{esc}, V_\mathrm{esc})$ is a uniform distribution in the range $[-V_\mathrm{esc}, V_\mathrm{esc}]$, and $\delta(x - x_\mathrm{GC})$ is a Dirac delta distribution centred on x_GC. We use a δ distribution because the uncertainty in the sky positions of the clusters is negligible. Finally, the likelihood of our model is given by the convolution of the DF with the $\mathcal{E}$ distribution of each cluster, which is

$$P(\boldsymbol{d}|\boldsymbol{\varpi}) = \prod_{i=0}^{N} \int \mathrm{d}\boldsymbol{u}\,\mathcal{E}(\boldsymbol{u}|\boldsymbol{d}_i)\,f[\boldsymbol{J}(\boldsymbol{u})]. \quad (A.6)$$

In practice, we evaluate Eq. (A.6) with a Monte Carlo method, sampling the integral and the $\mathcal{E}$ distribution of each cluster with 1000 realisations. Fortunately, the likelihood in Eq. (A.6) turns out to be quite insensitive to the specific form of both the density distribution ρ and the distributions of the missing velocities; in fact, we verified that using a Gaussian instead of a uniform distribution in v_x and v_y does not alter significantly our results on the halo masses. As an example, in Fig. 1d, we show the distribution of clusters around NGC 4494 on the observable projection of the phase space, the $V_\mathrm{los}{-}r$ plane, compared to the prediction of the maximum-likelihood $f(\boldsymbol{J})$ model for this galaxy. The $V_\mathrm{los}{-}r$ plane is effectively the sub-space where we are fitting our models to the data.

With the prior and likelihood defined as above, we evaluate the posterior distribution of the six free parameters of the model with an MCMC method; in particular, we use the affine-invariant sampler implemented in the code `emcee` by Foreman-Mackey et al. (2013). For all 25 SLUGGS early-type galaxies, we find that the chains converge quite rapidly around a well-defined peak in the posterior after a short burn-in phase. As an example, in Fig. 1c, we show the marginalised posterior distributions for the halo mass and concentration for the galaxy NGC 4494. Clearly, both M_h and c are well constrained by our analysis, despite having an unavoidable degeneracy. For each parameter, we take the median of the marginalised posterior as the best-fit value and the interval between the 16th and 84th percentiles as a measure of its uncertainty.

A.5. Derived quantities

From our model, with parameters optimised for each GC system in the SLUGGS sample, we can now derive several other properties of interest. In Fig. 1e, we show, as examples, the circular velocity curve of the mass distribution, V_circ, and the velocity anisotropy profile of the GC system, $\beta = 1 - (\sigma_\theta^2 + \sigma_\phi^2)/2\sigma_\mathrm{r}^2$. While V_circ depends only on the three free parameters of the gravitational potential ($M_\mathrm{h}, c, M/L_{3.6}$), β depends mostly on the three free parameters of the DF (ν_h, ν_g, J_0). This means, incidentally, that the uncertainty on V_circ, which we estimate with random realisations of the model from the posterior (1σ grey band in Fig. 1e), is fully determined by the width of the posterior on the parameters of the potential (Fig. 1c).

We can also compute the profile of the LOS velocity dispersion of the GC systems (σ_los), which depends on both the potential and the DF. We show this model profile for NGC 4494 in Fig. 1f, where we compare it with the observed profile (see Foster et al. 2016). Such a comparison is meaningful since we do not input directly the σ_los profile to our fitting routine, although we do, of

[7] We also recall that the potential is always more spherical than the mass distribution that it generates (Binney & Tremaine 2008).

course, input the same individual velocities that determine $\sigma_{\rm los}$. The agreement that we observe for NGC 4494 (Fig. 1f), and also for the other galaxies in our sample (not shown), thus serves as a useful consistency check on our procedure.

For 18 of the 25 early types in our sample, Pulsoni et al. (2018) measured the velocity dispersion profile of the population of planetary nebulae orbiting around the host galaxy and found that in most cases it agrees quite well with the $\sigma_{\rm los}$ profile of the GC system from SLUGGS. Figure 1f shows this agreement for NGC 4494. In a few cases, however, the $\sigma_{\rm los}$ for the planetary nebulae is ∼20−40% lower than for the GCs. This difference in the $\sigma_{\rm los}$ likely reflects the different density profiles of the two types of tracers orbiting in the same gravitational potential. Even among GCs, there are differences in $\sigma_{\rm los}$ when the system is subdivided by colour. Red GCs have lower $\sigma_{\rm los}$ than blue GCs, and are in better agreement with both the velocity dispersion of planetary nebulae and the stellar bodies of galaxies (e.g. Pota et al. 2015).

Appendix B: Model output for early-type galaxies

Table B.1. Output of our $f(\mathbf{J})$ model for the 25 early-type galaxies analysed in this work.

Name	log $M_\star/M_\odot$	log $M_{\rm h}/M_\odot$	c
NGC 720	11.27 ± 0.13	12.85 ± 0.32	7.1 ± 2.0
NGC 821	11.00 ± 0.13	13.00 ± 0.43	6.5 ± 1.8
NGC 1023	10.99 ± 0.12	12.98 ± 0.65	5.9 ± 1.8
NGC 1400	11.08 ± 0.13	12.71 ± 0.35	4.6 ± 1.3
NGC 1407	11.60 ± 0.13	13.70 ± 0.31	3.9 ± 1.0
NGC 2768	11.21 ± 0.13	12.60 ± 0.39	8.2 ± 2.5
NGC 2974	10.93 ± 0.12	12.71 ± 0.30	4.7 ± 1.1
NGC 3115	10.93 ± 0.14	13.01 ± 0.62	6.5 ± 2.1
NGC 3377	10.50 ± 0.13	12.22 ± 0.34	7.3 ± 1.9
NGC 3607	11.39 ± 0.12	13.08 ± 0.37	4.1 ± 1.1
NGC 3608	11.03 ± 0.12	13.15 ± 0.55	5.8 ± 1.6
NGC 4278	10.95 ± 0.13	13.40 ± 0.50	6.0 ± 1.7
NGC 4365	11.51 ± 0.13	13.84 ± 0.43	4.6 ± 1.2
NGC 4374	11.51 ± 0.14	13.69 ± 0.57	9.0 ± 2.8
NGC 4459	10.98 ± 0.11	12.82 ± 0.42	5.2 ± 1.4
NGC 4473	10.96 ± 0.12	12.88 ± 0.51	5.5 ± 1.7
NGC 4486	11.62 ± 0.14	13.75 ± 0.24	9.7 ± 1.8
NGC 4494	11.02 ± 0.12	12.35 ± 0.46	4.4 ± 1.3
NGC 4526	11.26 ± 0.13	13.16 ± 0.48	4.9 ± 1.2
NGC 4564	10.58 ± 0.12	12.88 ± 0.78	5.3 ± 2.0
NGC 4649	11.60 ± 0.13	13.76 ± 0.43	5.3 ± 1.4
NGC 4697	11.15 ± 0.12	13.17 ± 0.54	5.4 ± 1.6
NGC 5846	11.46 ± 0.13	13.85 ± 0.45	4.6 ± 1.1
NGC 5866	10.83 ± 0.13	12.06 ± 0.66	11.2 ± 5.5
NGC 7457	10.13 ± 0.24	12.02 ± 0.47	7.1 ± 2.3

Notes. The table provides estimates of the stellar mass ($M_\star$), the halo mass ($M_{\rm h}$), and the halo concentration (c) together with their 1-σ uncertainties.